



HAL
open science

Structure of Synthetic K-rich Birnessites Obtained by HighTemperature Decomposition of KMnO_4 . 2 Phase and Structural Heterogeneities

Anne-Claire Gaillot, Victor.A. Drits, Alain Plançon, Bruno Lanson

► **To cite this version:**

Anne-Claire Gaillot, Victor.A. Drits, Alain Plançon, Bruno Lanson. Structure of Synthetic K-rich Birnessites Obtained by HighTemperature Decomposition of KMnO_4 . 2 Phase and Structural Heterogeneities. *Chemistry of Materials*, 2004, 16, pp.1890-1905. 10.1021/cm035236r . hal-00193734

HAL Id: hal-00193734

<https://hal.science/hal-00193734>

Submitted on 4 Dec 2007

HAL is a multi-disciplinary open access archive for the deposit and dissemination of scientific research documents, whether they are published or not. The documents may come from teaching and research institutions in France or abroad, or from public or private research centers.

L'archive ouverte pluridisciplinaire **HAL**, est destinée au dépôt et à la diffusion de documents scientifiques de niveau recherche, publiés ou non, émanant des établissements d'enseignement et de recherche français ou étrangers, des laboratoires publics ou privés.

1 **Structure of Synthetic K-rich Birnessites Obtained by High-**
2 **Temperature Decomposition of KMnO₄.**

3 **III. Phase and Structural Heterogeneities**

4
5 **Anne-Claire Gaillot¹**

6 **Victor A. Drits^{1,2}**

7 **Alain Plançon³**

8 **Bruno Lanson^{1, *}**

9
10 1 – Environmental Geochemistry Group, LGIT – Maison des Géosciences, University of
11 Grenoble – CNRS, 38041 Grenoble Cedex 9, France.

12 2 – Geological Institute, Russian Academy of Sciences, 7 Pyzhevsky street, 109017
13 Moscow, Russia.

14 3 – Crystallography Laboratory, ISTO, University of Orléans - CNRS, 45067 Orléans
15 Cedex 2, France.

16
17 * Author to whom correspondence should be addressed.

18 e-mail : [Bruno.Lanson@obs.ujf-grenoble.fr](mailto: Bruno.Lanson@obs.ujf-grenoble.fr)

19

20

Abstract

21
22
23 Synthetic K-rich birnessites (KBi) were prepared from the thermal decomposition of a
24 fine-grained KMnO_4 powder heated in air atmosphere at temperatures ranging from 200-
25 1000°C . The qualitative analysis of powder X-ray diffraction (XRD) patterns reveals a
26 complex range of structural transformations from one metastable phase to the other, often
27 through intermediate mixed-layer structures (MLSs). Phase and structural heterogeneities of
28 KBi samples synthesized at 700°C , 800°C and 1000°C (referred to as KBi_7 , KBi_{8h} and
29 KBi_{10h}) have been studied in details by chemical and thermal analysis and by simulation of
30 the experimental powder XRD patterns. Two-layer orthogonal ($2O$), and hexagonal ($2H$) as
31 well as three-layer rhombohedral ($3R$) polytypes were identified in these samples. The $2O$
32 structure consists of vacancy-free layers and their orthogonal symmetry is linked to the high
33 content of layer Mn^{3+} cations and to the unique azimuthal orientation of Mn^{3+} octahedra
34 which are elongated because of Jahn-Teller distortion. In the $2H$ and $3R$ polytypes, the layers
35 have a hexagonal symmetry as they contain only Mn^{4+} - and vacant octahedra. As a result,
36 their interlayers have a heterogeneous cation composition, because of the migration of Mn^{3+}
37 from the layers to the interlayers. In addition to the periodic KBi polytypes, KBi_7 and KBi_{8h}
38 contain MLSs in which layer pairs of the $2H$ polytype are interstratified at random with those
39 of the $3R$ or of the $2O$ polytype. Interstratification of incommensurate $2O$ and $2H$ structural
40 fragments leads to peculiar diffraction effects and represents a new type of structural disorder
41 in birnessites. The increase of temperature from 700°C to 1000°C is associated with the
42 replacement of $3R/2H$, $2H$, and $2O/2H$ mixed-layered structures by the more stable $2O$
43 polytype. KBi_{10h} consists of a mixture of a minor $2H$ phase with three $2O$ varieties having
44 slightly different layer unit-cell parameters. This phase heterogeneity results from the partial
45 disorder in the orientation of Mn^{3+} octahedra. The average structural formulae,
46 $\text{K}^{+}_{0.265}\text{Mn}^{3+}_{0.145}(\text{Mn}^{4+}_{0.825}\square_{0.175})\text{O}_2 \cdot 0.68 \text{H}_2\text{O}$ for KBi_7 and KBi_{8h} , and

47 $\text{K}^{+}_{0.27}(\text{Mn}^{4+}_{0.77}\text{Mn}^{3+}_{0.21}\square_{0.02})\text{O}_2 \cdot 0.53 \text{H}_2\text{O}$ for $\text{KBi}_{10\text{h}}$, are in agreement with the main crystal
48 chemical features of the phases prevailing in these samples. When heated to 350°C , the $2O$
49 polytype presents a hexagonal layer symmetry with a b parameter (2.894 \AA) which is
50 significantly increased as compared to that determined at room temperature (2.850 \AA). Both
51 modifications arise from random orientation of elongated Mn^{3+} octahedra along directions
52 forming $n60^\circ$ angles with the a axis. The main factors responsible for the phase and structural
53 heterogeneity of the KBi samples are discussed.

54

55

Introduction

56

57 Layers building up hydrous manganese oxides such as birnessite consist of edge-sharing
58 MnO_6 octahedra. Hydrated exchangeable cations are present in the interlayer space to
59 compensate for the layer charge deficit arising from the presence within layers of Mn^{3+}
60 cations and/or of vacant layer octahedra.¹⁻⁶ Birnessite is easily synthesized under laboratory
61 conditions and some of the synthetic birnessite species have commonly been used as analogs
62 of the natural species to determine the structural mechanism of heavy metal sorption or to
63 investigate the structural modification of birnessite as a function of pH (e.g.).⁵⁻¹⁶
64 Simultaneously, synthetic birnessites have drawn a special attention as a potential cathode
65 material for secondary batteries following their intercalation with lithium cations.¹⁷⁻²¹ Because
66 of its apparent lamellar framework stability, K-rich birnessite (hereafter referred to as KBi)
67 represents a promising candidate as lithium battery cathode material. This birnessite variety
68 can be obtained from the thermal decomposition of KMnO_4 ,²¹ or of a mixture of MnO , KNO_3
69 and LiOH ,²² or from the Mn^{7+} reduction under hydrothermal conditions.^{19,20}

70 Because of their influence on reactivity it is essential to have a detailed understanding
71 of the structural and chemical features of these birnessite species. However, structural studies
72 of birnessite are most often impaired as these compounds occur normally in a finely dispersed

73 state. In addition, structural variety of birnessite is extreme as these species may differ from
74 each other by their layer symmetry, their layer stacking, or the content and distribution of
75 heterovalent Mn cations and layer vacancies within layers (e.g.). Furthermore, structural and
76 chemical defects, such as the interstratification of different layer types and stacking faults, are
77 frequent in these compounds.²³ As a result, only a few publications were devoted to the
78 structural study of KBi varieties. According to Chen et al.¹⁹ KBi variety synthesized under
79 hydrothermal conditions presents a three-layer rhombohedral (*3R*) structure in which
80 octahedral layers are shifted with respect to each other by $-a/3$ (assuming an orthogonal base-
81 centered unit cell) leading to the prismatic coordination of interlayer K coordinated to layer
82 oxygen atoms (O_{layer}). Kim et al.^{21,22} synthesized new high temperature KBi and K-Li
83 birnessite-like varieties with a two-layer polytype, in which adjacent layers are rotated with
84 respect to each other by 180° around the *c* axis passing through the layer Mn (Mn_{layer}) cations.
85 Even though the main idealized structural and chemical properties of high temperature KBi
86 have been determined,²¹ crystal chemistry of this new polytype and significant details of its
87 structure remain poorly understood.

88 In the two companion articles^{24,25} it is shown that KBi obtained from thermal
89 decomposition of $KMnO_4$ at 800°C and 1000°C have different unit cells and supercells,
90 different sources of the layer charge deficit and specific distribution of heterovalent Mn
91 cations. However, the two KBi samples described in these articles^{24,25} have a high structural
92 perfection and do not contain (KBi_{10o}) or contain only a few stacking faults (KBi_{8o}). In
93 contrast, the present article deals with phase, structural and chemical heterogeneity of KBi
94 varieties obtained at different temperatures and assesses the origin of such variability.
95 Specific structural and chemical heterogeneities are described for KBi and the original
96 methodology used to reveal these structural defects is detailed.

97

Main Structural Features of KBi_{80} and KBi_{100}

98

99

100 KBi samples with a high degree of structural order were obtained from thermal
101 decomposition of KMnO_4 at 800°C (KBi_{80}) and 1000°C (KBi_{100}) and their structure refined
102 from a single crystal²⁴ (KBi_{80}) or using the Rietveld method on a powder XRD pattern
103 (KBi_{100}).²⁵ As the present description of KBi structures relies for a large part on the structures
104 refined on these two samples, the main features of the refined models will be summarized.

105 Both samples have a two-layer unit cell in which adjacent layers are rotated with respect
106 to each other by 180° around the c axis passing through the Mn_{layer} cations. As a result of this
107 specific layer stacking mode, O_{layer} atoms from adjacent layers define in the interlayer region
108 prismatic cavities located above or below empty tridentate cavities, sharing three edges with
109 neighboring Mn_{layer} octahedra (TE sites).

110 However, extensive differences exist between the structure models refined for samples
111 KBi_{80} and KBi_{100} . The unit cell of sample KBi_{80} is hexagonal with $a = 2.840(1) \text{ \AA}$, and $c =$
112 $14.03(1) \text{ \AA}$, and space group $P6_3/mmc$. The hexagonal symmetry of the layer results from the
113 sole presence of Mn^{4+} in the octahedral layers, the presence of 0.12 vacant layer sites per
114 octahedron being responsible for the layer charge deficit.²⁴ This layer charge deficit is
115 compensated for 1) by the presence of 0.08 interlayer Mn^{3+} above or below vacant layer
116 octahedra sharing three O_{layer} with neighboring Mn_{layer} octahedra to form a triple-corner
117 surface complex ($^{\text{VI}}\text{TC}$ sites), and 2) by the presence of 0.24 interlayer K^+ in prismatic
118 cavities located above or below empty tridentate cavities, sharing three edges with
119 neighboring Mn_{layer} octahedra ($^{\text{VI}}\text{TE}$ sites).

120 Contrastingly, the amount of Mn^{3+} cations is much higher in the structure of KBi_{100}
121 (0.25 Mn^{3+} per octahedron) than in that of KBi_{80} (0.08 Mn^{3+} per octahedron). The systematic
122 presence of these cations in the octahedral sites of vacancy-free layers accounts for the layer
123 charge deficit, which is compensated by the sole presence of interlayer K^+ cations.²⁵ To

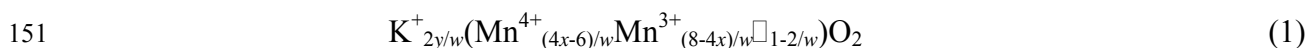
124 minimize steric strains within the octahedral layers of $\text{KBi}_{10\text{o}}$, heterovalent Mn_{layer} cations are
125 segregated in Mn^{3+} - and Mn^{4+} -rich rows parallel to $[010]$, and all Mn^{3+} -octahedra, which are
126 elongated because of Jahn-Teller distortion, present a unique azimuthal orientation. These two
127 features lead to the departure from the hexagonal layer symmetry, the unit cell of sample
128 $\text{KBi}_{10\text{o}}$ being orthogonal with $a = 5.155 \text{ \AA}$, $b = 2.846 \text{ \AA}$, $c = 14.09 \text{ \AA}$, and space group $Cmcm$.
129 In addition, the regular alternation along the a axis of each Mn^{3+} -rich row with two Mn^{4+} -
130 rows, emphasized by the associated distribution of interlayer cations, gives rise to a supercell
131 with $A = 3a$.

132 133 **Experimental** 134

135 KBi samples were prepared from the thermal decomposition of fine-grained KMnO_4
136 powder (particle size $< 50 \mu\text{m}$) in air following the modified procedure of Kim et al.²¹ In the
137 companion papers^{24,25} a flat crucible covered by a thin layer of KMnO_4 powder (100-
138 $180\text{mg}/\text{cm}^2$) was used for the pyrolysis to form homogeneous and highly periodic structures.
139 In the present article high-temperature (800-1000°C) pyrolysis were performed with crucibles
140 containing a thick layer of KMnO_4 (Table 1). At lower temperature (200-700°C), pyrolysis
141 was performed using a flat crucible covered by a thin layer of KMnO_4 (Table 1).
142 Heterogeneous KBi samples synthesized at 200°C, 400°C, 600°C, 700°C, 800°C and 1000°C
143 for the present study will hereafter be referred to as KBi_2 , KBi_4 , KBi_6 , KBi_7 , $\text{KBi}_{8\text{h}}$, and
144 $\text{KBi}_{10\text{h}}$. Details on the processing of pyrolysis products, as well as on the thermal and
145 chemical analyses are given by Gaillot et al.²⁴

146 The mean oxidation degree of manganese in birnessite was determined by
147 potentiometric titration using $(\text{NH}_4)_2\text{Fe}(\text{SO}_4)$ Mohr salt and sodium pyrophosphate.^{26,27}
148 Knowing the mean oxidation state, $2x$, and the atomic K/Mn ratio determined by ICP, y , it is

149 possible to calculate an average structural formula for a given KBi sample using the following
150 equation²⁴:



152 where $w = (2x + y) / 2$.

153 The amount of interlayer water may be introduced in this structural formula using the
154 DTA and DTG data.

155 Powder XRD patterns were recorded using a Bruker D5000 powder diffractometer
156 equipped with a Kevex Si(Li) solid detector and $\text{CuK}\alpha_{1+2}$ radiation. Intensities were recorded
157 from 5 to 90° at a 0.04° 2 θ interval using a 40 sec counting time per step. Full widths at half
158 maximum intensity (FWHM) were determined for diffraction maxima using the standard
159 EVA program available from Bruker. A rotating sample holder was used for room
160 temperature data collections to minimize preferential orientation effects. A TTK450 Anton
161 Paar chamber was used to record XRD patterns from samples heated *in situ*.

162
163 **Simulation of Powder XRD Patterns.** In the present study, samples with both high
164 phase heterogeneity and high proportion of structural defects have been investigated. As
165 compared to the KBi_{80} and KBi_{100} samples described in the two companion papers^{24,25} the
166 combination of these two intrinsic features impairs the ability to find a suitable single crystal
167 and would dramatically reduce the representativeness of this crystal. These features also
168 strongly reduce the efficiency of usual structure refinement methods including the Rietveld
169 method. One of the most effective ways to determine the actual structure of defective layered
170 compounds is the calculation of XRD patterns using the mathematical formalism described in
171 detail by Drits and Tchoubar.²³ This trial-and-error procedure has been used successfully to
172 determine the crystal-chemical structure of different natural and synthetic birnessites
173 consisting of commensurate layers in the *ab* plane.^{12-16,28} Details on the program used to
174 calculate XRD patterns, and on the fitting procedure are given by Plançon²⁹ and Drits et al.,¹³

175 respectively. For birnessites in which partially incommensurate layers are interstratified, the
 176 mathematical formalism described by Plançon²⁹ was used. The fit quality was estimated over
 177 the 34°-56° 2θ CuKα range using the usual R_{wp} parameter. XRD patterns calculations were
 178 restricted to 20ℓ and 11ℓ reflections (indexing based on an orthogonal base-centered unit cell)
 179 because these lines are most sensitive to structural parameters of layered minerals, including
 180 order/disorder and stacking sequences.³⁰ For each sample, the background was assumed to be
 181 linearly decreasing over the considered angular range, and preferred orientation of particles
 182 was considered as a variable parameter.

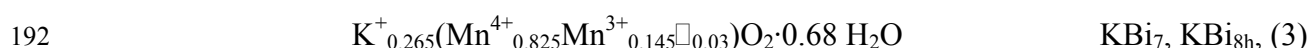
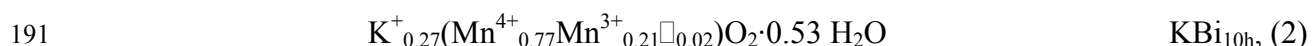
183

184

Results

185

186 **Structural Formulae of KBi Samples.** K/Mn atomic ratios determined for KBi₇, KBi_{8h}
 187 and KBi_{10h} are similar (0.270, 0.274 and 0.271, respectively) whereas the mean oxidation
 188 degree of Mn is lower for KBi_{10h} (3.78) than for KBi₇ and KBi_{8h} (3.87 and 3.85 – Table 2).
 189 From these analytical results, and the experimentally determined structural water weight
 190 losses (Table 2) the following formulae may be deduced from Equation (1):



193

194 **Main Features of the Experimental Powder XRD Patterns.** XRD patterns collected
 195 for KBi samples synthesized at temperatures ranging 200-1000°C all exhibit basal reflections
 196 at ~7.13 Å and ~3.56 Å characteristic of the layered structure of birnessite (Figure 1).
 197 However, the profiles of these basal reflections, as well as the number, the position, the
 198 FWHM, the profiles and the relative intensities of *hkl* reflections differ significantly from one
 199 pattern to the other (Figure 1). These differences are indicative of the structure contrast
 200 between the different samples. For example, KBi₂ possesses a turbostratic structure as its

201 XRD pattern contains only basal reflections and un-modulated two-dimensional 20,11 and
202 31,02 diffraction bands. KBi_4 also has very a low degree of structural order as its XRD pattern
203 only contains, in addition to 20,11 and 31,02 diffraction bands, two very broad modulations at
204 37.3 and $42.1^\circ 2\theta$ $\text{CuK}\alpha$ (2.410 and 2.145 Å, respectively). From 600°C and up, XRD patterns
205 of KBi samples exhibit well-defined, sharp and intense hkl reflections whose position shifts
206 and intensity distribution modifications reflect the evolution of the KBi structure as a function
207 of synthesis temperature. Structural and crystal-chemical features of KBi samples synthesized
208 at 700-1000°C will be detailed below. To differentiate the homogeneous samples obtained at
209 800° and 1000°C and described by Gaillot et al. from the heterogeneous KBi_{10h} and KBi_{8h}
210 samples described in the present paper, the former ones will hereafter be referred to as KBi_{10o}
211 and KBi_{8o} .^{24,25}

212
213 **Indexation of the Experimental Powder XRD Patterns.** All XRD patterns were
214 indexed using base-centered orthogonal unit cells independently of their hexagonal ($a = b\sqrt{3}$)
215 or orthogonal ($a > b\sqrt{3}$) layer symmetry. Therefore, reflections located in the 34° - 70° 2θ
216 $\text{CuK}\alpha$ range have $20\ell, 11\ell$ indices and $31\ell, 02\ell$ ones in the 64° - 70° 2θ $\text{CuK}\alpha$ range.

217 *KBi_{10h} .* In the 34° - 56° 2θ range, two sets of non-basal reflections may be distinguished
218 (Figures 1, 2). The first one consists of intense and sharp reflections (2.485, 2.347, 2.204,
219 2.040, 1.718 Å) which can be indexed using a hexagonal two-layer (2H) unit cell, with $a =$
220 4.976 Å, $b = 2.873$ Å, $c = 14.240$ Å, $\alpha = \beta = \gamma = 90^\circ$ ($a = b\sqrt{3}$ – Table 3). The second set
221 includes weaker and broader reflections (2.552, 2.404, 2.249, 2.074, 1.738 Å), systematically
222 located on the low angle side of the strong reflections of the first set. The common indexation
223 of the two sets of reflections leads to an orthogonal two-layer (2O) unit cell, with $a = 5.101$ Å,
224 $b = 2.850$ Å, $c = 14.240$ Å, $\alpha = \beta = \gamma = 90^\circ$, and $a/b = \sqrt{3.21}$ (Table 3), these parameters
225 being similar to those obtained for KBi_{10o} ($a = 5.155$ Å, $b = 2.846$ Å, $c = 14.088$ Å, $\alpha = \beta =$

226 $\gamma = 90^\circ$). For this orthogonal cell, intense and weak reflections have 11ℓ and 20ℓ indices,
227 respectively. Even though unit-cell parameters of $\text{KBi}_{10\text{h}}$ and $\text{KBi}_{10\text{o}}$ are similar the intensity
228 ratio between 20ℓ and 11ℓ reflections is much lower for $\text{KBi}_{10\text{h}}$. The weakness of 20ℓ
229 reflections could be related to the physical mixture of hexagonal $2H$ and orthogonal $2O$
230 varieties in $\text{KBi}_{10\text{h}}$. The presence of the $2O$ variety is attested by the presence of 020 and 310
231 reflections at 1.425 Å and 1.460 Å, respectively (Table 3). In contrast, the presence of the $2H$
232 variety remains uncertain because the 310,020 reflection at 1.436 Å is not clearly visible in
233 the experimental XRD pattern of $\text{KBi}_{10\text{h}}$. However, the broad maximum observed at 1.431 Å
234 could result from the overlap of the 310,020 reflection of the $2H$ phase ($d = 1.436$ Å) and of
235 the 312 and 020 reflections of the $2O$ phase ($d = 1.430$ Å, and 1.425 Å, respectively – Figures
236 1, 2, Table 3).

237 *KBi_{8h}*. The three sharp peaks present at 1.448 Å, 1.426 Å and 1.398 Å (Figure 2), can be
238 indexed with two different unit cells. The first one has an orthogonal layer symmetry and a
239 two-layer periodicity along the c axis with $a = 5.060$ Å, $b = 2.855$ Å, $c = 14.200$ Å, whereas
240 the second one considers a hexagonal layer symmetry with $a_{\text{ort}} = a_{\text{hex}}\sqrt{3} = 4.945$ Å, $b_{\text{ort}} =$
241 $b_{\text{hex}} = 2.855$ Å, $c = 14.320$ Å. However, $d(20\ell, 11\ell)$ values calculated for these two unit cells
242 are systematically shifted with respect to the experimental ones (Table 4). Such a systematic
243 disagreement between calculated and experimental d -values could possibly indicate a physical
244 mixture of the $2H$ and $2O$ birnessite varieties. In such case, the observed discrepancy between
245 the experimental and calculated peak positions may result from the overlap of the $2H$ and $2O$
246 reflections which usually sandwich experimental maxima. However, the positions of 20ℓ lines
247 determined experimentally for the $2O$ variety should strictly coincide with those calculated
248 for this polytype. On the contrary, these experimental positions are systematically shifted
249 towards the positions calculated for the $11\ell, 20\ell$ reflections of the $2H$ variety. As a
250 consequence, the systematic disagreement between the experimental and calculated peak
251 positions most likely results from the coexistence within $\text{KBi}_{8\text{h}}$ coherent scattering domains

252 (CSDs) of layer fragments from both *2H* and *2O* varieties. In this case, specific diffraction
253 effects should result from the interstratification of partially incommensurate layers, shifting
254 11ℓ and 20ℓ reflections, changing their relative intensity and modifying their profiles as
255 described by Drits et al.,^{13,31} and Lanson et al.¹⁴ In addition to these structural varieties, $\text{KBi}_{8\text{h}}$
256 sample contains a 3-layer rhombohedral (*3R*) birnessite-like polytype as indicated by the
257 presence of three weak peaks at 2.412 Å, 2.144 Å, and 1.817 Å (Figure 2) which correspond
258 respectively to 112, 115 and 118 reflections of this *3R* phase (see description of KBi_7).

259 *KBi₇*. As for $\text{KBi}_{8\text{h}}$, reflections were indexed using both *2H* and *2O* unit cells with
260 $a = 4.945$ Å, $b = 2.855$ Å, $c = 14.320$ Å, $\alpha = \beta = \gamma = 90^\circ$ ($a = b\sqrt{3}$), and $a = 5.060$ Å, $b =$
261 2.855 Å, $c = 14.200$ Å, $\alpha = \beta = \gamma = 90^\circ$, respectively. As for the $\text{KBi}_{8\text{h}}$ sample, the d -values
262 calculated for ($20\ell, 11\ell$) reflections of the *2H* phase are systematically shifted with respect to
263 experimental ones towards those calculated for the *2O* unit cell (Table 4). Similarly, the three
264 maxima at 2.410 Å, 2.143 Å and 1.818 Å, were indexed with a *3R* unit cell with $a = 4.945$ Å,
265 $b = 2.855$ Å, $c = 21.420$ Å, $\alpha = \beta = \gamma = 90^\circ$ (112, 115 and 118 reflections, respectively).

266 *Powder XRD Patterns of Heated KBi Samples*. Additional XRD patterns were recorded
267 *in situ* from $\text{KBi}_{10\text{h}}$ and $\text{KBi}_{8\text{h}}$ samples heated to 350°C under air conditions (Figure 3). For
268 both patterns, reflections are indexed with a two-layer hexagonal (*2H*) unit cell with $a =$
269 4.980 Å, $b = 2.875$ Å, $c = 12.995$ Å (350- $\text{KBi}_{8\text{h}}$), and $a = 5.013$ Å, $b = 2.894$ Å, $c = 12.920$ Å
270 (350- $\text{KBi}_{10\text{h}}$), $\alpha = \beta = \gamma = 90^\circ$, and $a = b\sqrt{3}$ (Table 5).

271

272 **FWHM of 20ℓ and 11ℓ Reflections as a Function of ℓ .** For three-dimensional (3D)
273 periodic structures, peak broadening has two main sources.³² Crystal-size broadening
274 originates from the small CSD size and leads to an increase of the FWHM values proportional
275 to $1/\cos\theta$. Strains or fluctuations of the unit cell parameters represent the second possible
276 source of peak broadening and lead to a FWHM increase proportional to $\tan\theta$. After
277 correction for either of these factors, FWHM of the reflections with identical hk values should

278 be similar. Accordingly, for the defect-free $\text{KBi}_{10\text{o}}$ sample, FWHM values of 20ℓ and 11ℓ
279 reflections are almost independent of ℓ or slightly increase with ℓ after correction by $\cos\theta$
280 (Figure 4). For $\text{KBi}_{10\text{h}}$ on the other hand, FWHM values dramatically decrease with ℓ for 20ℓ
281 reflections. Such a decrease of peak breadth with ℓ should not be observed for strictly periodic
282 structures.

283
284 **Simulation of $\text{KBi}_{10\text{h}}$ Powder XRD Pattern.** In agreement with the model proposed by
285 Kim et al.²¹ and further refined by Gaillot et al.²⁴, it is assumed that the two-layer periodicity
286 of the $\text{KBi}_{10\text{h}}$ structure results from the rotation of adjacent layers by 180° around the c axis
287 passing through Mn_{layer} . As determined for different synthetic birnessites^{5,13-16,21} including
288 $\text{KBi}_{8\text{o}}$ and $\text{KBi}_{10\text{o}}$ ^{24,25} it is assumed that the thickness of octahedral layers is 2.00 \AA , and that
289 Mn cations are located in the center of MnO_6 octahedra. As in sample $\text{KBi}_{10\text{o}}$,²⁵ O_{layer} atoms
290 are shifted along the a axis as compared to the ideal anion close packing site ($0.341 a$ Vs.
291 $0.333 a$ – Table 6) and K^+ cations are located above or below the empty tridentate cavity. This
292 site is actually split, each of the split positions being shifted in the ab plane from the center of
293 the prismatic cavity defined by O_{layer} of adjacent layers towards one of its faces.^{24,25} Similarly,
294 interlayer H_2O molecules are located in the middle of the interlayer space in-between two
295 O_{layer} from adjacent layers but slightly shifted along the a axis towards the nearest Mn_{layer}
296 (Figure 5). Optimal coordinates of the layer and interlayer sites leading to the fits shown in
297 Figure 6 are listed in Table 6 together with their occupancies, whereas selected interatomic
298 distances are given in Table 7.

299 As compared to the experimental XRD pattern collected for $\text{KBi}_{10\text{h}}$, the one calculated
300 for a defect-free $2O$ structure with $a_1 = 5.101 \text{ \AA}$, $b_1 = 2.850 \text{ \AA}$, $c = 14.240 \text{ \AA}$ exhibits 20ℓ
301 maxima which are sharper and more intense than experimental ones in contrast to 11ℓ
302 reflections (Figure 6a). To increase the FWHM of 20ℓ reflections and to decrease their

303 intensity, KBi_{10} is assumed to integrate several $2O$ modifications having slightly different a
 304 and b parameters but keeping the same c parameter. To keep profiles and intensities of 11ℓ
 305 reflections these unit-cell parameters are related by the following relation:

$$306 \quad \frac{1}{d^2(110)} = \frac{1}{a_i^2} + \frac{1}{b_i^2} \quad (4)$$

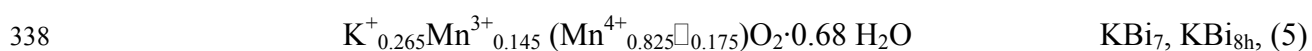
307 The position of 11ℓ reflections is unchanged for each $2O$ modifications whose a and b
 308 parameters verify Equation (4). On the other hand, 20ℓ reflections of these modifications are
 309 slightly shifted to higher or lower 2θ values by decreasing or increasing their a parameter, and
 310 increasing or decreasing their b parameter, respectively. Figure 6b compares the experimental
 311 XRD pattern obtained for KBi_{10h} with those calculated for three defect-free $2O$ modifications
 312 having slightly different layer unit-cell parameters. The XRD pattern calculated for a mixture
 313 of these three modifications exhibits 11ℓ reflections similar to those in each elementary XRD
 314 pattern, whereas 20ℓ reflections are significantly broadened, as observed in KBi_{10h}
 315 experimental pattern. In addition, intensity and positions of the 11ℓ reflections in KBi_{10h}
 316 experimental pattern are similar to those of $20\ell, 11\ell$ reflections calculated for a $2H$
 317 modification with $a = 4.976 \text{ \AA}$, $b = 2.873 \text{ \AA}$ and $c = 14.240 \text{ \AA}$ (Figure 6c).

318 Finally, the best possible fit to the experimental KBi_{10h} XRD pattern (Figure 6d – $R_{wp} =$
 319 11.1%) was obtained for a physical mixture of three $2O$ modifications ($a_1 = 5.124 \text{ \AA}$, $b_1 =$
 320 2.846 \AA , $a_2 = 5.101 \text{ \AA}$, $b_2 = 2.850 \text{ \AA}$, and $a_3 = 5.084 \text{ \AA}$, $b_3 = 2.853 \text{ \AA}$ – $c = 14.240 \text{ \AA}$) and of a
 321 $2H$ phase with $a = 4.976 \text{ \AA}$, $b = 2.873 \text{ \AA}$, and $c = 14.240 \text{ \AA}$. Relative proportions of these
 322 different phases are 32, 31, 13, and 24%, respectively.

323
 324 **Powder XRD Pattern Simulation for KBi_{8h} and KBi_7 .** From the indexation of
 325 experimental XRD patterns, the description of KBi_{8h} and KBi_7 samples as a physical mixture
 326 of various KBi polytypes devoid of well-defined stacking faults may be rejected.
 327 Accordingly, all attempts to fit the experimental XRD patterns as a physical mixture of

328 periodic $2H$, $2O$ and $3R$ polytypes failed. Alternatively, KBi_{8h} and KBi_7 samples can be
 329 described a mixture of elementary phases each consisting of interstratified fragments of $2H$,
 330 $2O$ and $3R$ polytypes. Such interstratification may shift 11ℓ and 20ℓ reflections, change their
 331 relative intensity and modify their profiles as described by Drits et al.,^{13,31} and Lanson et al.¹⁴

332 *Structure of Elementary $2O$, $2H$, and $3R$ Fragments.* Atomic positions and occupancies
 333 of the various sites in the interstratified $2O$ and $2H$ fragments are assumed to be similar to
 334 those refined for KBi_{10o} using the Rietveld method²⁵ and for KBi_{8o} from a single crystal.²⁴
 335 Occupancies of these sites are set according to KBi_{8h} structural formulae (Eq. 3). However,
 336 this formula should be modified to account for the migration of Mn^{3+} cations from layer to
 337 interlayer in the $2H$ structure and for the resulting presence of vacant octahedra²⁴:



339 However, the contrasting layer symmetry in the $2H$ and $2O$ varieties most likely results
 340 from different contents of Mn^{3+} cations in the KBi structure.^{24,25} From the two structure
 341 models proposed by these authors, the Mn^{3+} content is indeed much lower in the $2H$ variety
 342 than in the $2O$ one. In turn, these contrasting Mn^{3+} contents give rise to different ways to
 343 minimize the steric strains arising from the elongation of Mn^{3+} octahedra, and lead in the first
 344 case to the departure of Mn^{3+} cations from layer to the interlayer ($2H$ – lower Mn^{3+} content),
 345 and in the second case to an ordered distribution of Mn^{3+} cations within vacancy-free layers
 346 ($2O$ – higher Mn^{3+} content). As a consequence, the proposed structural formula, which is
 347 calculated from the mean chemical parameters determined on the bulk KBi_{8h} sample, averages
 348 the relative contributions of $2H$ and $2O$ varieties, which are likely closer to the models
 349 proposed by Gaillot et al.^{24,25}

350 In the $2H$ variety, the site for interlayer H_2O is split to provide an octahedral
 351 coordination to interlayer Mn^{3+} cations on the one hand and, on the other hand, to ensure H-
 352 bonds with O_{layer} of adjacent octahedral Mn layers as in the $2O$ variety. In both $2O$ and $2H$
 353 polytypes, the $\text{K}_{\text{interlayer}}$ site is split as described for KBi_{10h} (Figure 5). Atomic positions and

354 occupancies of the $2H$ ($a = 4.945 \text{ \AA}$, $b = 2.855 \text{ \AA}$, $c = 14.320 \text{ \AA}$) and $2O$ ($a = 5.043 \text{ \AA}$, $b =$
355 2.850 \AA , $c = 14.240 \text{ \AA}$) cells providing the best fit to the experimental XRD patterns are given
356 in Table 8. For the sake of simplicity, atomic positions and occupancies in the layers and
357 interlayers of the $3R$ polytype are assumed to be identical to those in the $2H$ one.

358 *Diffraction Effects Resulting from the Interstratification of Elementary $2O$, $2H$, and $3R$*
359 *Fragments.* $2O$ and $2H$ fragments consists of two octahedral layers rotated with respect to
360 each other by 180° around the c axis passing through Mn_{layer} site, and will be hereafter
361 referred to as A and B fragments, respectively. These fragments differ by their a parameter
362 (5.060 \AA and 4.945 \AA , respectively) whereas they have the same b parameter (2.855 \AA). As a
363 result, interstratified $2O/2H$ structures consist of partly incommensurate A and B fragments. In
364 addition, in such interstratified structures, the interlayer structure depends on the sequence of
365 structural fragments. For example in an AB sub-sequence, the first and third interlayers are
366 identical to those in the $2O$ and $2H$ polytypes, respectively, whereas the second interlayer has
367 an intermediate structure corresponding to a "mixed" $2O$ and $2H$ interlayer (Figure 7).

368 As mentioned before, in the $3R$ polytype octahedral layers are shifted with respect to the
369 previous one by $-a/3$ along the a axis. Such layer pairs are hereafter referred to as C fragments
370 and are assumed to have layer and interlayer structures similar to those in B fragments (Table
371 8). B and C fragments are stacked without displacement in the ab plane in BB and BC sub-
372 sequences whereas they are shifted with respect to each other by $-a/3$ along the a axis in CB
373 and CC sub-sequences (Figure 7b).

374 The comparison of $\text{KBi}_{8\text{h}}$ experimental pattern with that calculated for a randomly
375 interstratified $2O/2H$ (60:40) mixed-layered structure (MLS – Figure 8b) shows that such
376 interstratification induces a significant alteration of 20ℓ reflection profiles. With increasing ℓ
377 values the 20ℓ maxima appear as shoulders on the low angle side of corresponding 11ℓ
378 reflections (Figure 8b). Similarly, when looking at XRD patterns calculated for $3R/2H$ MLSs
379 containing 75% and 15% of $2H$ layer pairs (Figures 8d, f, respectively) $20\ell, 11\ell$ reflections are

380 located between the corresponding reflections of the defect-free $2H$ and $3R$ polytypes in
381 agreement with the conceptual model proposed by Drits et al.³¹ These authors showed that for
382 a random interstratification of layers fragments having similar thickness but different
383 interlayer displacements observed hkl reflections are located between neighboring hkl
384 reflections of phases whose layer fragments are interstratified, the exact position depending
385 on the relative proportion of the elementary components.

386 *Description of KBi_{8h} and KBi_7 Samples as a Mixture of Defective KBi Phases.* The best
387 fit to the experimental KBi_{8h} XRD pattern (Figure 9a – $R_{WP} = 8.2\%$) was obtained for a
388 mixture of the defect-free $2H$ polytype with interstratified $2O/2H$, $2H/3R$ and $3R/2H$ MLSs
389 containing respectively 40%, 75% and 15% of hexagonal layer pairs in a 9:34:48:8 ratio. The
390 quality of the fit shown on Figure 11a pleads for a realistic description of KBi_{8h} structural
391 heterogeneity. However, this quality relies on a significant number of adjusted parameters and
392 the actual presence of each of the four elementary phases needs to be assessed. The respective
393 contributions of these different MLSs to the diffracted intensity are shown on Figures 9b-d
394 which compare the experimental KBi_{8h} pattern with those calculated for models similar to the
395 optimal one from which one of the contributions is systematically modified or subtracted. As
396 a result of these structural modifications, the quality of fit is systematically deteriorated in
397 specific parts of the calculated diagram, and more specifically in the high intensity
398 "background" regions between the main reflections, supporting the existence of each of these
399 elementary phases.

400 The best fit to the experimental KBi_7 pattern (Figure 10a – $R_{WP} = 9.1\%$) was obtained
401 for a mixture in a 7:29:41:23 ratio of defect-free $2H$ polytype with interstratified $2O/2H$ and
402 $2H/3R$ and $3R/2H$ MLSs containing respectively 50%, 70%, and 10% of hexagonal layer
403 pairs. The respective contributions of each of these elementary phases to the diffracted
404 intensity are shown on Figures 10b-d which compare the experimental KBi_7 XRD pattern
405 with those calculated for models similar to the optimal one from which one of the

406 contributions is systematically modified or subtracted. As for sample $\text{KBi}_{8\text{h}}$, the quality of fit
407 is then systematically deteriorated in specific parts of the experimental diagram, and more
408 specifically in the high intensity "background" regions between the main reflections,
409 supporting the existence of each of these elementary phases.

410

411 Discussion

412

413 **Phase and Structural Heterogeneity of KBi .** The results obtained in the present article
414 and in the companion papers^{24,25} show that phase and structural heterogeneity of KBi samples
415 synthesized at 800°C and 1000°C strongly depends on the heterogeneity of physico-chemical
416 conditions (temperature, PO_2 , ...) within the KMnO_4 powder during the synthesis at these
417 elevated temperatures. Homogeneous KBi samples are obtained when flat crucibles covered
418 by a very thin layer of KMnO_4 powder are used. For example by heating a flat crucible
419 covered with a thin layer of KMnO_4 powder ($\sim 180 \text{ mg.cm}^{-2}$) to 1000°C a unique defect-free
420 $2O$ phase is obtained (sample $\text{KBi}_{10\text{o}}$).²⁵ If the thickness of the layer of KMnO_4 powder is
421 increased as for the synthesis of $\text{KBi}_{10\text{h}}$ ($\sim 475 \text{ mg.cm}^{-2}$), the resulting product contains various
422 $2O$ varieties with slightly different unit-cell parameters (Table 9).

423 Similarly, at 800°C phase heterogeneity increases with the thickness of the layer of
424 KMnO_4 powder. In particular, the decomposition of a thin layer of KMnO_4 powder
425 (100 mg.cm^{-2}) covering a flat crucible leads to the formation of the defect-free $2H$ phase in
426 sample $\text{KBi}_{8\text{o}}$ which contains in addition a defective interstratified $3R/2H$ phase. Increasing
427 the layer thickness of KMnO_4 powder up to 955 mg.cm^{-2} leads to a dramatic increase of phase
428 heterogeneity as observed for $\text{KBi}_{8\text{h}}$ sample (Figure 9, Table 10), most likely reflecting
429 temperature or PO_2 heterogeneity within the KMnO_4 powder during the synthesis.

430

431 **Structure of KBi as a Function of Synthesis Temperature.** Synthetic analogues of
432 birnessites are usually obtained at low-to-medium temperatures, that is between 5°C^{1,2,11,33}
433 and 200-500°C.^{19,20,34,35} Kim et al.²¹ assumed that a significant increase of temperature, up to
434 1000°C, would promote the formation of birnessite-like compounds having a high structural
435 perfection and a high density, which are essential parameters for the phase stability required
436 in their sought electrochemical application. These authors were the first to obtain high-
437 temperature KBi by using K⁺ as interlayer cations to prevent the formation of Mn oxides with
438 tunnel or anion close-packed structures (pillaring effect), and highly oxidizing conditions to
439 prevent the transition towards mixed-valence oxides. As a result, a variety of synthetic
440 birnessite in which successive layers are rotated with respect to each other by 180° around the
441 *c* axis was obtained.^{21,22,24,25} However, the structural characterization of KBi samples obtained
442 at 800°C and 1000°C temperatures was confined to the determination of idealized models,^{21,22}
443 and additional insights in the KBi structure will be provided below.

444 *Layer Stacking and Symmetry.* Our experimental work and results show that
445 temperature plays a key decisive role in the occurrence of the different layer stacking modes,
446 as well as for layer and interlayer composition. A temperature increase from 200°C to 1000°C
447 results in a complex sequence of structural transitions from one metastable phase to the other
448 through intermediate mixed-layered varieties. At 400°C, the turbostratic stacking of KBi₂ is
449 replaced by a highly disordered 3*R* polytype. The structural order of this 3*R* phase increases
450 significantly by increasing temperatures to 600-700°C as attested by the presence of sharp and
451 intense reflections (112_R, 115_R and 118_R) which are diagnostic for this phase (Figure 1). In
452 addition, these temperatures (600-700°C) correspond to the onset of the 2*H* polytype
453 formation, the proportion of which increases at the expense of the 3*R* phase with increasing
454 temperature.

455 The detailed phase characterization of KBi samples obtained at temperatures higher
456 than 600°C reveals the main trends of phase transitions affecting KBi structures. With this

457 respect, the composition of KBi_7 and KBi_8 samples is especially remarkable as both samples
458 contain the same four main phases. However the temperature increase from 700°C to 800°C
459 leads to significant modifications between the two samples. The overall tendency is the
460 decreasing proportion of the $3R$ layer pairs with increasing temperature and the related
461 increase of $2H$ and $2O$ layer pair proportions (Figure 11 – Table 10). This tendency is
462 systematically observed in the four constituting phases as the proportion of $2H$ layer pairs
463 increases from 70 to 75% in the $2H/3R$ MLS and from 10 to 15% in the $3R/2H$ MLS when
464 increasing the pyrolysis temperature from 700 to 800°C . In addition, the proportion of $2O$
465 layer pairs in the $2O/2H$ MLS increases from 50% in KBi_7 to 60% in KBi_8 , the relative
466 proportion of this $2O/2H$ MLS increasing slightly from KBi_7 to KBi_{8h} at the expense of the
467 $3R/2H$ MLS (Table 10). At higher temperature (1000°C) $3R$ layer pairs are absent and the
468 sample is overwhelmingly dominated by the $2O$ polytype (Table 10). In KBi_{10h} phase
469 heterogeneity is minimum as the defect-free $2O$ phase makes up most of the sample together
470 with a minor amount (24%) of a defect-free $2H$ phase.

471 *Layer Structure.* Difference in KBi formation temperature modifies not only the layer
472 stacking mode but also the crystal chemistry of KBi layers and interlayers. In particular, a
473 temperature increase from 800°C to 1000°C leads to a much higher proportion of Mn^{3+}
474 cations in the structure (0.14 in KBi_{8h} as compared to 0.24 in KBi_{10h}). The contrasting amount
475 of Mn^{3+} cations is combined with distinct distributions of these cations between layer and
476 interlayer sites in the two varieties, as described earlier for the ordered KBi_{8o} and KBi_{10o}
477 samples.^{24,25} In KBi_{8o} interlayer Mn^{3+} cations are located above or below vacant layer
478 octahedra in $^{\text{VI}}\text{TC}$ sites, whereas they are present in the octahedral sites of vacancy-free layers
479 in KBi_{10o} . In this latter variety, the unique azimuthal orientation of Mn^{3+} -octahedra, which are
480 elongated because of Jahn-Teller distortion, leads to the departure from the hexagonal layer
481 symmetry. However, by heating this variety up to 350°C it is possible to obtain a random
482 orientation of elongated Mn^{3+} octahedra as described by Gaillot et al.²⁵ Mn^{3+} -containing

483 layers of edge-sharing MnO_6 octahedra may have hexagonal symmetry such as in
484 lithiophorite as a result of this random orientation with respect to the a axis ($n60^\circ$ rotations) of
485 Mn^{3+} octahedra. In addition to considerable lattice strains, such azimuthal distribution of
486 Mn^{3+} octahedra leads to increased b parameters (2.925 Å in lithiophorite³⁶) as compared to
487 those determined for birnessites whose layers are devoid of Mn^{3+} cations or for birnessites
488 with an ordered distribution of heterovalent Mn octahedra. For these two birnessite families
489 the experimentally determined b parameters range 2.844 – 2.854 Å.^{6,13-16,24,25}

490 Accordingly, XRD patterns recorded for samples $\text{KBi}_{8\text{h}}$ and $\text{KBi}_{10\text{h}}$ heated *in situ* at
491 350°C (350- $\text{KBi}_{8\text{h}}$ and 350- $\text{KBi}_{10\text{h}}$, respectively) may be indexed with a unique $2H$ phase with
492 a b parameter equal to 2.875 Å and 2.894 Å, respectively. It should be noted that the unit-cell
493 parameters obtained for sample $\text{KBi}_{10\text{o}}$ heated *in situ* at 350°C ($b = 2.895$ Å and $c = 12.848$ Å)
494 ²⁵ almost coincide with those determined for $\text{KBi}_{10\text{h}}\text{-350}$ sample ($b = 2.894$ Å and $c =$
495 12.920 Å – Table 9) pleading for a similar content of $\text{Mn}^{3+}_{\text{layer}}$ in the two samples. The
496 different b parameters determined for 350- $\text{KBi}_{8\text{h}}$ and 350- $\text{KBi}_{10\text{h}}$ are in agreement with the
497 contrasting contents of $\text{Mn}^{3+}_{\text{layer}}$ in the two samples. From the comparison of Equations 2 and
498 5, an even stronger contrast is expected as hexagonal layers of $\text{KBi}_{8\text{h}}$ are presumably devoid
499 of Mn^{3+} . However $2O$ layer pairs, which contain a significant amount of $\text{Mn}^{3+}_{\text{layer}}$ (Table 8),
500 represent 19% of $\text{KBi}_{8\text{h}}$ sample and will contribute to a significant increase of the average b
501 parameter in the $2O/2H$ phase (Figure 10 – Table 10), leading in turn to the increase of the b
502 parameter observed when heating sample $\text{KBi}_{8\text{h}}$ to 350°C.

503 In both $\text{KBi}_{8\text{h}}$ and $\text{KBi}_{10\text{h}}$, the $2O$ polytype and A structural fragments consist of
504 vacancy-free layers, whereas layers of the $2H$ and $3R$ polytypes, as well as B and C structural
505 fragments, contain a significant proportion of vacant layer sites (up to 0.15 per octahedron –
506 Tables 6, 8). These vacant octahedra originate mostly from the migration of Mn^{3+} cations
507 from the layer to the interlayer. As a result, $2O$, $2H$ and $3R$ structures have contrasting
508 interlayer compositions and different distributions of these interlayer species. The interlayers

509 of the $2O$ layer pairs are homogeneous and contain only K^+ cations and associated H_2O
510 molecules, whereas the interlayers of the $2H$ and $3R$ fragments are heterogeneous as they
511 contain octahedrally coordinated Mn^{3+} cations along with K^+ cations and H_2O molecules.

512

513 **KBi Heterogeneity and FWHM of Reflections in Experimental Powder XRD**

514 **Patterns.** FWHM values measured for 20ℓ and 11ℓ reflections of KBi_{10o} and for 11ℓ maxima
515 of sample KBi_{10h} are almost independent of ℓ (Figure 4). In contrast, FWHM values measured
516 for 20ℓ reflections of KBi_{10h} dramatically decrease with increasing ℓ values. To account for
517 such a contrasting behavior between 11ℓ and 20ℓ reflections of KBi_{10h} , one has to consider
518 that KBi_{10h} consists of several $2O$ varieties with slightly different a and b parameters but
519 identical $d(110)$ values. As a consequence, 11 rods corresponding to these different varieties
520 coincide in the reciprocal lattice, whereas their 20 rods are located close to each other along
521 the a^* axis. These latter rods are not strictly superimposed but partially overlap each other.

522 Diffraction effects arising from this particular case are described below. Powder X-ray
523 diffraction effects are conventionally derived in the reciprocal space from the rotation of the
524 reciprocal lattice with respect to a fixed Ewald sphere. Brindley and Méring proposed an
525 alternative and effective view in which the reciprocal lattice is fixed and the radius of Ewald
526 sphere is continuously increased.³⁷ In this alternative model, the integrated intensity at $1/d$
527 sums up intensities of the reciprocal lattice nodes located on the surface of the Ewald sphere
528 having a $1/d$ radius. This alternative approach may be used to predict reflection profiles for a
529 physical mixture of two phases having closely related a and b unit-cell parameters. The
530 reciprocal lattice of a layered structure may be represented as a set of hk rods parallel to the c^*
531 axis along which $hk\ell$ nodes with different ℓ values are located (Figure 12a).²³ Two partially
532 overlapping reciprocal rods having the same hk indices and containing reflections with the
533 same ℓ values are shown on Figure 12b together with the Ewald spheres defining $hk\ell$
534 reflections for these two reciprocal rods. With increasing ℓ values, the two rods contribute

535 simultaneously to the diffracted intensity over an increased range of $1/d$ values. This leads to
536 a shorter distance between the respective maxima corresponding to the two overlapping
537 reflections (dashed lines – Figure 12b) and to a lower FWHM for the resulting combined
538 diffraction maximum (Figure 12b) as observed experimentally after correction for crystal-size
539 broadening. The observed decrease of the 20ℓ reflection FWHM with increasing ℓ values
540 (Figure 4) can thus be considered as an independent evidence of such type of phase
541 heterogeneity. Because all $2O$ varieties have identical $d(110)$ values, 11 reciprocal rods
542 completely overlap in the reciprocal space and, as a consequence, the FWHM of 11ℓ
543 reflections is independent of ℓ despite the differences in a and b parameters. One may note
544 (Figure 4) that for the homogeneous KBi_{10o} sample the correlations between FWHM and ℓ for
545 20ℓ and 11ℓ reflections lead to slightly different slopes. This difference most likely reflects
546 the presence in this sample of a small proportion of particles having $2O$ structure and unit-cell
547 parameters slightly different from those of the main $2O$ phase. The relation between the
548 FWHM of $11\ell, 20\ell$ reflection and the ℓ indice may be used as an independent criterion to
549 estimate the degree of phase heterogeneity in KBi samples.

550

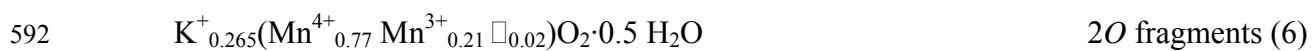
551 **Origin of the Structural Heterogeneity for KBi_{10h} .** Heterogeneous heating to
552 $\sim 1000^\circ\text{C}$ of individual KMnO_4 particles leads essentially to the formation of KBi crystals
553 having different a and b parameters. The a/b ratios obtained for the three identified sub-
554 populations of KBi crystals range 1.784-1.800 (Table 9) as a consequence of lattice distortion
555 induced by the Jahn-Teller distortion of Mn^{3+} octahedra. Two hypotheses may account for the
556 observed scatter of the a/b ratio. The first one is the local fluctuation of the redox conditions
557 in which individual KBi crystals are formed resulting in the presence of contrasting amounts
558 of Mn^{3+} cations from one crystal to the other. According to the other hypothesis, all KBi
559 crystals have almost the same content of Mn^{3+} cations but differ from each other by their
560 respective mean orientation of the long $\text{Mn}^{3+}\text{-O}$ bonds with respect to the a axis. In this

561 second hypothesis, the maximum a/b ratio likely correspond to crystals in which most or all
562 Mn^{3+} octahedra are elongated along the a axis, whereas in crystals with the minimum a/b ratio
563 the long Mn^{3+} -O bonds of some Mn^{3+} octahedra are likely oriented at $\pm 60^\circ$ with respect to the
564 a axis. Such different azimuthal orientations of elongated Mn^{3+} octahedra should result in an
565 increased b parameter whereas the a parameter should decrease, as observed experimentally.
566 After heating to $350^\circ C$ the FWHM of $11\ell, 20\ell$ reflections recorded for 350-KBi_{10o} and 350-
567 KBi_{10h} are almost independent of ℓ (Figure 13) pleading for a similar content of Mn^{4+} and
568 Mn^{3+} in all KBi_{10h} crystals, as in KBi_{10o}. The similar unit-cell parameters obtained for 350-
569 KBi_{10o} and 350-KBi_{10h} (2.894 Å vs. 2.895 Å, respectively) also support this second
570 hypothesis of a partial disorientation of Mn^{3+} octahedra with respect to the a axis. It should be
571 noted that the presence of the $2H$ polytype, even though minor, does not affect the FWHM of
572 $11\ell, 20\ell$ reflections recorded for 350-KBi_{10h}. This is likely due to the presence of a relatively
573 high amount of Mn^{3+}_{layer} in the layers building up this $2H$ polytype (Table 6). This hypothesis
574 is supported by the high value (2.873 Å – Table 9) determined for the b parameter of this $2H$
575 polytype. As discussed above, such a high b parameter most likely results from the random
576 orientation of elongated Mn^{3+} octahedra within the octahedral layer of birnessite.

577

578 **Origin of the Structural Heterogeneity for KBi_{8h}.** KBi_{8h} is a complex physical
579 mixture of a periodic $2H$ phase and of various $2O/2H$ and $3R/2H$ MLSs. In these different
580 phases, individual layers have different layer symmetry most likely resulting from contrasting
581 contents of Mn^{3+}_{layer} . As described above, A fragments likely consist of vacancy-free layers
582 containing a significant amount of Mn^{3+}_{layer} (~25%) whereas B and C fragments are likely
583 devoid of Mn^{3+}_{layer} cations as a result of their layer-to-interlayer migration. As can be seen in
584 Figure 13, the FWHM values measured for 350-KBi_{8h} sample decrease systematically with
585 increasing ℓ values to indicate the coexistence of crystals with close but different unit-cell
586 parameters as described above. The difference of unit-cell parameters after heating to $350^\circ C$

587 and the induced random orientation of elongated Mn^{3+} octahedra likely originates from the
 588 coexistence of crystals with contrasting contents of Mn^{3+} layer. By combining chemical data
 589 (Equations 3 and 5) and structural details derived from XRD simulations (Table 8), it is
 590 possible to propose the following structural formulae for *2O* fragments on the one hand and
 591 for *2H* and *3R* ones on the other hand:



594 The resulting mean oxidation degree Mn ($3.79 \times 19\% + 3.88 \times 81\% = 3.86$) is
 595 compatible with that determined experimentally (3.85 – Table 1) by combining chemical data
 596 (Equations 3 and 5) and structural details derived from XRD.

597

598 **New Type of Structural Disorder in Birnessite.** Except for the frequent presence of
 599 random stacking faults, two types structural defects are extremely common in layered
 600 structures. The random interstratification of layers having different thicknesses, which is the
 601 first type of such structural disorder, is especially widespread in mixed-layered clay
 602 minerals.³⁸ Well defined stacking faults, which make the other type of structural disorder, are
 603 conveniently described as resulting from the interstratification of layers having similar
 604 thickness but different interlayer displacements.³¹

605 The random interstratification of *2O* (*A*) and *2H* (*B*) structural fragments in the *2O/2H*
 606 phase described in both KBi_7 and KBi_{8h} represents a new type of structural disorder in
 607 lamellar structures. In this specific case, interstratified layers have the same thickness and the
 608 same interlayer stacking mode, but their layer dimensions in the *ab* plane are
 609 incommensurate. Such crystal structures consisting of alternating layers having different unit-
 610 cell parameters have been previously reported in the literature. For example, alternation of
 611 incommensurate layers has been described in the structures of asbolanes,³⁹ valleriite and
 612 tochilinite.⁴⁰⁻⁴² However, in all these "hybrid structures"⁴⁰ incommensurate layers are

613 regularly alternating along the c axis and their structures may be described by a set of unit
614 cells, which have not only different sizes but also different shapes.

615 In contrast, the $2O$ and $2H$ structural fragments having different a parameters are
616 randomly interstratified in the $2O/2H$ phase, and the description of the diffraction effects by
617 such a structure should be analogous to that developed for mixed-layered structures^{23,43,44} and
618 for the structures containing stacking faults.^{23,29,45} In the reciprocal space, 11 rods of the
619 interstratified fragments completely overlap each other because of their identical $d(110)$
620 values leading to the coherence of the diffracted waves for 11ℓ reflections. A similar effect
621 exists for the 20ℓ and 11ℓ reflections of the hexagonal fragments as these reflections coincide
622 with 11ℓ reflections of the $2O$ fragments. Such a high coherence gives rise to the sharp and
623 intense maxima observed for the combined $20\ell, 11\ell$ reflections of the $2H$ fragments and 11ℓ
624 reflections of the $2O$ fragments (Figures 2, 9, 10). In contrast, a significant phase misfit arises
625 for the incomplete overlap of 20 rods from $2O$ fragments with those of the $2H$ fragments
626 leading to a significant loss of coherence of the diffracted waves when $2O$ and $2H$ fragments
627 are interstratified. As a result, 20ℓ reflections of the $2O$ fragments are broadened and shifted
628 towards the partially overlapped $20\ell, 11\ell$ and 11ℓ reflections scattered by the $2H$ and $2O$ layer
629 pairs, respectively, and are only observed as diffuse shoulders (Figures 9, 10).

630

631 **Acknowledgements**

632

633 VAD is grateful to the Environmental Geochemistry Group of the LGIT (Grenoble,
634 France) and to the Russian Science Foundation for financial support. BL acknowledges
635 financial support from INSU/Géomatériaux, and CNRS/PICS709 programs. Céline Boissard
636 (Hydr'ASA – Poitiers), Martine Musso and Delphine Tisserand (LGIT – Grenoble) are
637 thanked for their technical support (DT-TG analyses and chemical analyses, respectively).

638

Literature cited

- 639
640
- 641 (1) Giovanoli, R.; Stähli, E.; Feitknecht, W. *Helv. Chim. Acta* **1970**, *53*, 209-220.
- 642 (2) Giovanoli, R.; Stähli, E.; Feitknecht, W. *Helv. Chim. Acta* **1970**, *53*, 453-464.
- 643 (3) Burns, R. G.; Burns, V. M. *Phil Trans Roy Soc London A* **1977**, *286*, 283-301.
- 644 (4) Chukhrov, F. V.; Gorschkov, A. I.; Rudnitskaya, E. S.; Sivtsov, A. V. *Izv. Akad. Nauk Geol.* **1978**, *9*, 67-76.
- 645
- 646 (5) Post, J. E.; Veblen, D. R. *Amer. Mineral.* **1990**, *75*, 477-489.
- 647 (6) Drits, V. A.; Silvester, E. J.; Gorshkov, A. I.; Manceau, A. *Amer. Mineral.* **1997**, *82*, 946-961.
- 648
- 649 (7) Drits, V. A.; Lanson, B.; Bougerol Chaillout, C.; Gorshkov, A. I.; Manceau, A. *Amer. Mineral.* **2002**, *87*, 1646-1661.
- 650
- 651 (8) Manceau, A.; Schlegel, M. L.; Chateigner, D.; Lanson, B.; Bartoli, C.; Gates, W. P. In *Synchrotron X-ray methods in clay science*; Schulze, D. G., Stucki, J. W., Bertsch, P. M., Eds.; Clay Minerals Society: Boulder, Co, 1999; Vol. 9, pp 68-114.
- 652
- 653
- 654 (9) Manceau, A.; Lanson, B.; Drits, V. A. *Geochim. Cosmochim. Acta* **2002**, *66*, 2639-2663.
- 655
- 656 (10) Kuma, K.; Usui, A.; Paplawsky, W.; Gedulin, B.; Arrhenius, G. *Miner. Mag.* **1994**, *58*, 425-447.
- 657
- 658 (11) Silvester, E. J.; Manceau, A.; Drits, V. A. *Amer. Mineral.* **1997**, *82*, 962-978.
- 659 (12) Manceau, A.; Drits, V. A.; Silvester, E. J.; Bartoli, C.; Lanson, B. *Amer. Mineral.* **1997**, *82*, 1150-1175.
- 660
- 661 (13) Drits, V. A.; Lanson, B.; Gorshkov, A. I.; Manceau, A. *Amer. Mineral.* **1998**, *83*, 97-118.
- 662
- 663 (14) Lanson, B.; Drits, V. A.; Silvester, E. J.; Manceau, A. *Amer. Mineral.* **2000**, *85*, 826-838.
- 664

- 665 (15) Lanson, B.; Drits, V. A.; Feng, Q.; Manceau, A. *Amer. Mineral.* **2002**, *87*,
666 1662-1671.
- 667 (16) Lanson, B.; Drits, V. A.; Gaillot, A. C.; Silvester, E.; Plançon, A.; Manceau, A.
668 *Amer. Mineral.* **2002**, *87*, 1631-1645.
- 669 (17) Le Goff, P.; Baffier, N.; Bach, S.; Pereira-Ramos, J. P.; Messina, R. *Solid State*
670 *Ionics* **1993**, *61*, 309-315.
- 671 (18) Le Goff, P.; Baffier, N.; Bach, S.; Pereira-Ramos, J.-P. *J. Mater. Chem.* **1994**,
672 *4*, 875-881.
- 673 (19) Chen, R. J.; Zavalij, P.; Whittingham, M. S. *Chem. Mater.* **1996**, *8*, 1275-1280.
- 674 (20) Chen, R. J.; Chirayil, T.; Zavalij, P.; Whittingham, M. S. *Solid State Ionics*
675 **1996**, *86-88*, 1-7.
- 676 (21) Kim, S. H.; Kim, S. J.; Oh, S. M. *Chem. Mater.* **1999**, *11*, 557-563.
- 677 (22) Kim, S. H.; Im, W. M.; Hong, J. K.; Oh, S. M. *J. Electrochem. Soc.* **2000**, *147*,
678 413-419.
- 679 (23) Drits, V. A.; Tchoubar, C. *X-ray diffraction by disordered lamellar structures:*
680 *Theory and applications to microdivided silicates and carbons*; Springer-Verlag: Berlin,
681 1990.
- 682 (24) Gaillot, A.-C.; Drits, V. A.; Flot, D.; Manceau, A.; Burghammer, M.; Lanson,
683 B. *Chem. Mater.* **2003**, *15*, 4666-4678.
- 684 (25) Gaillot, A.-C.; Drits, V. A.; Lanson, B.; Manceau, A. *Chem. Mater.* **2004**, *In*
685 *preparation*.
- 686 (26) Vetter, K. J.; Jaeger, N. *Electrochim. Acta* **1966**, *11*, 401-419.
- 687 (27) Lingane, J. J.; Karplus, R. *Ind. Eng. Chem. Anal. Ed.* **1946**, *18*, 191-194.
- 688 (28) Chukhrov, F. V.; Sakharov, B. A.; Gorshkov, A. I.; Drits, V. A.; Dikov, Y. P.
689 *Int. Geol. Rev.* **1985**, *27*, 1082-1088.
- 690 (29) Plançon, A., Ph. D. Thesis, Orléans, France, 1976.

- 691 (30) Brindley, G. W. In *Crystal Structures of Clay Minerals and their X-ray*
692 *Identification*; Brindley, G. W., Brown, G., Eds.; Mineralogical Society: London, 1980, pp
693 125-195.
- 694 (31) Drits, V. A.; McCarty, D. K. *Amer. Mineral.* **1996**, *81*, 852-863.
- 695 (32) Klug, H. P.; Alexander, L. E. *X-ray diffraction procedures for polycrystalline*
696 *and amorphous materials*; Wiley: New York, 1974.
- 697 (33) Bach, S.; Pereira-Ramos, J. P.; Baffier, N. *J. Solid State Chem.* **1995**, *120*, 70-
698 73.
- 699 (34) Ching, S.; Roark, J. L.; Duan, N.; Suib, S. L. *Chem. Mater.* **1997**, *9*, 750-754.
- 700 (35) Ching, S.; Landrigan, J. A.; Jorgensen, M. L.; Duan, N.; Suib, S. L.; O'Young,
701 C. L. *Chem. Mater.* **1995**, *7*, 1604-1606.
- 702 (36) Post, J. E.; Appleman, D. E. *Amer. Mineral.* **1988**, *73*, 1401-1404.
- 703 (37) Brindley, G. W.; Méring, J. *Acta Crystallogr.* **1951**, *4*, 441-447.
- 704 (38) Moore, D. M.; Reynolds, R. C., Jr *X-ray Diffraction and the Identification and*
705 *Analysis of Clay Minerals*; Oxford University Press, 1989.
- 706 (39) Chukhrov, F. V.; Gorshkov, A. I.; Drits, V. A. *Izv. Akad. Nauk Geol.* **1982**, *6*,
707 69-77 (in Russian).
- 708 (40) Evans, H. T.; Allman, R. Z. *Kristallogr.* **1968**, *127*, 73-93.
- 709 (41) Drits, V. A. *Electron diffraction and high-resolution electron microscopy of*
710 *mineral structures*; Springer Verlag: Berlin Heidelberg, 1987.
- 711 (42) Organova, N. I.; Drits, V. A.; Dimitrik, A. L. *Amer. Mineral.* **1974**, *59*, 190-
712 200.
- 713 (43) Drits, V. A.; Sakharov, B. A. *X-Ray structure analysis of mixed-layer minerals*;
714 Nauka: Moscow, 1976.

715 (44) Reynolds, R. C., Jr In *Crystal structures of clay minerals and their X-ray*
716 *identification*; Brindley, G. W., Brown, G., Eds.; The Mineralogical Society: London, 1980,
717 pp 249-359.

718 (45) Plançon, A. *J. Appl. Cryst.* **1981**, *14*, 300-304.

719

720

Figure captions

721

722 **Figure 1.** Experimental XRD patterns of KBi samples obtained from thermal decomposition
723 of KMnO_4 at temperatures varying from 1000°C to 200°C (from top to bottom). Dashed lines
724 outline the position of 00ℓ reflections, whereas dot-dashed lines indicate the positions of
725 reflections of KBi 3R polytype. Intensity scale is enlarged over the $30\text{-}80^\circ 2\theta$ $\text{CuK}\alpha$ range.

726 **Figure 2.** Experimental XRD patterns of KBi samples obtained from thermal decomposition
727 of KMnO_4 at temperatures varying from 1000°C to 700°C (from top to bottom). Dashed lines
728 outline the position of 31ℓ and 02ℓ reflections, whereas dot-dashed lines indicate the positions
729 of reflections of KBi 3R polytype. Diffraction maxima are indexed in terms of the $2O$, $2H$ and
730 $3R$ polytypes identified in these samples (Tables 3 and 4).

731 **Figure 3.** Experimental XRD patterns of $\text{KBi}_{10\text{h}}$ (top) and $\text{KBi}_{8\text{h}}$ (bottom) samples recorded *in*
732 *situ* at 350°C . Diffraction maxima are indexed in terms of the $2H$ polytype identified in these
733 samples (Table 5). Stars indicate the 11ℓ reflections of a 3R-type phase as listed in Table 5.

734 **Figure 4.** Evolution of the full width at half maximum intensity (FWHM) for 20ℓ and 11ℓ
735 reflections (circles and triangles, respectively) as a function of the Miller index ℓ . FWHM are
736 corrected by $\cos\theta$. Homogeneous $\text{KBi}_{10\text{o}}$ ²⁵ and heterogeneous $\text{KBi}_{10\text{h}}$ samples are shown
737 respectively at the top and the bottom.

738 **Figure 5.** Structure model for $\text{KBi}_{10\text{h}}$. **a)** Projection on the ab plane. The upper surface of the
739 lower layer is shown as light shaded triangles. O_{layer} and Mn_{layer} of this lower layer are shown
740 as small solid and large open circles, respectively. Large shaded circles = interlayer

741 potassium. Interlayer H₂O molecules are shown as large open circles with a dashed outline. **b)**
742 Projection along the *b* axis. Open and solid symbols indicate atoms at $y = 0$, and at $y = \pm 1/2$,
743 respectively. Small circles represent O_{layer} atoms, large circles represent Mn_{layer} atoms, squares
744 represent vacant layer octahedra. Dot-dashed lines outline the interlayer prisms defined by the
745 two empty tridentate layer cavities. The center of these prisms is shown by regular dashed
746 lines, and the arrow outlines the shift of K cations from this ideal position.

747 **Figure 6.** Comparison between experimental and calculated XRD patterns for KBi_{10h}.
748 Experimental data are shown as crosses, whereas calculated profiles are shown as solid lines.
749 Only 20ℓ and 11ℓ reflections are calculated. Atomic coordinates and other structural
750 parameters used for the calculations are listed in Tables 6, 9, and 10. **(a)** Calculation for a
751 unique $2O$ polytype ($2O_2$). **(b)** Calculation made assuming the presence of three $2O$ polytypes
752 having slightly different unit-cell parameters. $2O_1$, $2O_2$, and $2O_3$, are shown as dashed, solid,
753 and dot-dashed lines, respectively. **(c)** Calculation made for a $2H$ polytype. **(d)** Optimum
754 model and difference plot.

755 **Figure 7.** Schematic view along the *b* axis of the interlayer structure in mixed-layered
756 structures (MLSs) of different KBi polytypes. Interlayers of the $2O$ polytype (A fragments)
757 are shown as small solid circles, whereas those of $2H$ and $3R$ polytypes (B and C fragments,
758 respectively) are shown as small solid triangles. Respective orientations of successive layers
759 in the different polytypes are schematized by the orientations of Mn octahedra in projection
760 along the *b* axis. The increased *a* parameter of the A fragments, as compared to B and C
761 fragments, is symbolized by the elongation of projected Mn octahedra. $2O/2H$ and $2H/3R$
762 MLSs are described in the top and bottom parts of the figure, respectively.

763 **Figure 8.** Comparison between experimental and calculated XRD patterns for KBi_{8h}. Patterns
764 as in Figure 6. Only 20ℓ and 11ℓ reflections are calculated. Atomic coordinates and other
765 structural parameters used for the calculations are listed in Tables 8 and 9. **(a)** Calculation
766 made for a defect-free $2O$ phase. **(b)** Calculation made for a $2O/2H$ MLSs ($2O:2H$ ratio

767 60:40). (c) Calculation made for a defect-free $2H$ phase. (d) Calculation made for a $2H/3R$
768 MLSs ($2H:3R$ ratio 75:25). (e) Calculation made for a $3R/2H$ MLSs ($3R:2H$ ratio 85:15). (f)
769 Calculation made for a defect-free $3R$ phase.

770 **Figure 9.** Comparison between experimental and calculated XRD patterns for KBi_{8h} . Patterns
771 as in Figure 6. Only 20ℓ and 11ℓ reflections are calculated. Atomic coordinates and other
772 structural parameters used for the calculations are listed in Tables 8, 9, and 10. Arrows outline
773 the misfits between experimental and calculated patterns. (a) Optimum model and difference
774 plot. The optimum model includes contributions from a defect-free $2H$ polytype and from
775 $2O/2H$, $2H/3R$, and $3R/2H$ MLSs (Relative proportions 9:34:48:8 – Table 10). (b) Calculation
776 made replacing the optimum $2O/2H$ contribution ($2O:2H$ ratio 60:40) by a defect-free $2H$
777 contribution. (c) Calculation made by subtracting the $2H/3R$ contribution ($2H:3R$ ratio 75:25)
778 from the optimum model. (d) Calculation made by subtracting the $3R/2H$ contribution ($3R:2H$
779 ratio 85:15) from the optimum model.

780 **Figure 10.** Comparison between experimental and calculated XRD patterns for KBi_7 . Patterns
781 as in Figure 6. Only 20ℓ and 11ℓ reflections are calculated. Atomic coordinates and other
782 structural parameters used for the calculations are listed in Tables 8, 9, and 10. Arrows outline
783 the misfits between experimental and calculated patterns. (a) Optimum model and difference
784 plot. The optimum model includes contributions from a defect-free $2H$ polytype and from
785 $2O/2H$, $2H/3R$, and $3R/2H$ MLSs (Relative proportions 7:29:41:23 – Table 10). (b)
786 Calculation made replacing the optimum $2O/2H$ contribution ($2O:2H$ ratio 50:50) by a defect-
787 free $2H$ contribution. (c) Calculation made by subtracting the $2H/3R$ contribution ($2H:3R$ ratio
788 70:30) from the optimum model. (d) Calculation made by subtracting the $3R/2H$ contribution
789 ($3R:2H$ ratio 90:10) from the optimum model.

790 **Figure 11.** Relative proportions of $3R$, $2H$, and $2O$ layer pairs (solid bars, shaded bars, and
791 open bars, respectively) in KBi samples as a function of the pyrolysis temperature.

792 **Figure 12.** (a) Schematic description of the intensity diffracted at a hkl node (shaded
793 ellipsoid) by the intersection of a hk rod (dot-dashed cylinder) with Ewald spheres (radii
794 ranging $1/d'-1/d''$). The distribution of intensity within the hkl node is schematized by the
795 intensity of the gray shading. (b) Schematic description of the intensity diffracted at two
796 partially overlapping hkl nodes (shaded cylinders) by the intersection of hk rods (with dot-
797 dashed and solid outlines, respectively) with Ewald spheres of increasing radii. The positions
798 of hkl reflections barycenters are outlined by dashed lines. On the right side of the figure the
799 breadth of resulting hkl reflection is shown as a function of the z^* coordinate along the c^*
800 axis. Reflection broadening with increasing z^* coordinate resulting from the intensity
801 distribution within the hkl node is not represented.

802 **Figure 13.** Evolution of the FWHM for 20ℓ , 11ℓ reflections as a function of the Miller index
803 ℓ . FWHM of the $K\alpha_2$ -stripped lines are corrected by $\cos\theta$. Heterogeneous 350-KBi_{8h},
804 heterogeneous 350-KBi_{10h}, and homogeneous 350-KBi_{10o}²⁵ samples are shown as solid
805 diamonds, solid triangles, and solid squares, respectively.

Table 1. Experimental conditions (shape and size of crucible and density of KMnO_4 powder) used for the synthesis of the KBi samples.

Sample	Amount of KMnO_4 powder	Surface area (crucible)	Density of powder (mg/cm^2)
$\text{KBi}_{10\text{o}}$ (homogeneous) ^a	2g	$4.5 \times 2.5 \text{ cm}^2$	178
$\text{KBi}_{10\text{h}}$	1.5g	$\pi \times 1^2 \text{ cm}^2$	477
$\text{KBi}_{8\text{o}}$ (homogeneous) ^b	3g	$6.8 \times 4.45 \text{ cm}^2$	100
$\text{KBi}_{8\text{h}}$	3g	$\pi \times 1^2 \text{ cm}^2$	955
KBi_7	1g	$4.5 \times 2.5 \text{ cm}^2$	89
KBi_6	2g	$\pi \times 2.25^2 \text{ cm}^2$	126
KBi_4	2g	$\pi \times 2.25^2 \text{ cm}^2$	126
KBi_2	2g	$\pi \times 2.25^2 \text{ cm}^2$	126

Note: ^a Sample described by Gaillot et al.²⁵ ^b Sample described by Gaillot et al.²⁴

Table 2. Main chemical parameters of KBi samples

	KBi_7	$\text{KBi}_{8\text{h}}$	$\text{KBi}_{10\text{h}}$
Weight loss due to interlayer H_2O	6.3%	6.5%	8.9%
Weight loss due to hydroxyl groups	2.6%	2.3 %	-
$\text{H}_2\text{O}/\text{Mn}$ ratio	0.70	0.68	0.53
K/Mn ratio	0.270	0.274	0.271
Mn mean oxidation state	3.87	3.85	3.78

Note: K/Mn ratio is determined by ICP-AES. Weight losses correspond to the first two endotherms ($\sim 150^\circ\text{C}$ and 370°C , respectively) observed on the DTA-TG curves. $\text{H}_2\text{O}/\text{Mn}$ ratio includes both interlayer H_2O and hydroxyl groups.

Table 3. Indexing of the experimental XRD pattern of $\text{KBi}_{10\text{h}}$ with $2O$ and $2H$ cells.

$d_{\text{exp}} (hkl)$	$2H$ polytype		$2O$ polytype	
	hkl	$d_{\text{cal}} (hkl)$	hkl	$d_{\text{cal}} (hkl)$
7.705 ^a				
7.131	002	7.120	002	7.120
4.404 ^a				
3.700 ^a				
3.562	004	3.560	004	3.560
2.750 ^a				
2.552			200	2.551
2.485	200, 110	2.488	110	2.488
2.451	201, 111	2.451	111	2.451
2.404			202	2.401
2.347	202, 112	2.349	112	2.349
2.249			203	2.247
2.204	203, 113	2.204	113	2.204
2.074			204	2.073
2.040	204, 114	2.039	114	2.039
1.898			205	1.900
1.874	205, 115	1.874	115	1.874
1.781	008	1.780	008	1.780
1.738			206	1.737
1.718	206, 116	1.717	116	1.717
1.460			208 / 310	1.460
1.448	208, 118	1.448	118	1.448
1.431	310, 020	1.436	312	1.430
1.425			020	1.425
1.397	312, 022	1.408	022	1.397
1.352			314	1.351
1.344			209	1.345
1.334	209, 119	1.335	119	1.335
	314, 024	1.332		
1.323			024	1.323
1.243	220, 400	1.244	220 / 316	1.244
			20.10	1.243
1.236	221, 401	1.239	221 / 11.10	1.239 / 1.236
1.225	316, 026	1.229		
	222, 402	1.225	222 / 026	1.225 / 1.222
1.204	223, 403	1.203	223	1.203
1.174	224, 404	1.174	224	1.174
1.128			318 / 406	1.129 / 1.123
1.102	226, 406	1.102	226	1.102

Note: $a = 4.976 \text{ \AA}$, $b = 2.873 \text{ \AA}$, $c = 14.240 \text{ \AA}$, $\alpha = \beta = \gamma = 90^\circ$ ($2H$ polytype), and $a = 5.101 \text{ \AA}$, $b = 2.850 \text{ \AA}$, $c = 14.240 \text{ \AA}$, $\alpha = \beta = \gamma = 90^\circ$ ($2O$ polytype). Calculated $d_{\text{cal}} (hkl)$ reflection positions (in \AA) are compared to experimental $d_{\text{exp}} (hkl)$ ones. ^a indicates additional lines related to the supercell of the $2O$ polytype.²⁵

Table 4. Indexing of the experimental XRD patterns of KBi_{8h} and KBi_7 with $2O$, $2H$, and $3R$ cells.

KBi_7	KBi_{8h}	$2H$ polytype		$2O$ polytype		$3R$ polytype	
$d_{\text{exp}} (hkl)$	$d_{\text{exp}} (hkl)$	hkl	$d_{\text{cal}} (hkl)$	hkl	$d_{\text{cal}} (hkl)$	hkl	$d_{\text{cal}} (hkl)$
7.140	7.136	002	7.160	002	7.110	003	7.140
3.574	3.567	004	3.580	004	3.555	006	3.570
2.514	2.517			200	2.530		
2.479				110	2.487		
2.471	2.472	200, 110	2.473				
2.456				111	2.449	201	2.456
	2.428	201, 111	2.436				
2.410	2.412					112	2.409
2.378	2.378	006	2.387	202, 006	2.384, 2.370	009	2.380
2.341	2.342	202, 112	2.337	112	2.347		
2.223	2.218			203	2.232	204	2.245
2.195	2.196	203, 113	2.195	113	2.202		
2.143	2.144					115	2.141
	2.058			204	2.061		
2.036	2.036	204, 114	2.034	114	2.038		
1.929						207	1.923
1.871	1.871	205, 115	1.872	115	1.872		
1.818	1.817					118	1.816
1.785	1.785	008	1.790	008	1.778	00.12	1.785
	1.728			206	1.730		
1.717	1.717	206, 116	1.717	116	1.716		
1.626						20.10	1.619
1.531						11.11	1.530
1.448	1.448	208, 118	1.450	208, 310, 118	1.454, 1.452, 1.446		
1.426	1.426	310, 020	1.427	020, 312	1.428, 1.423	310, 020	1.427
1.416				00.10	1.422		
1.399	1.398	312, 022	1.400	022	1.400	313, 023	1.400
1.340	1.338	209, 119	1.338	314, 119	1.344, 1.332		
1.325	1.325	314, 024	1.326	024	1.325	316, 026	1.325
1.235	1.237	20.10, 11.10	1.238	316	1.238		
		400, 220	1.236	11.10	1.234	221	1.234
		316, 026	1.225	222	1.225	402	1.228
1.223	1.222	402, 222	1.218	026	1.223	319, 029	1.224
1.191	1.190	403, 223	1.197	404	1.192	224	1.205
1.169	1.170	404, 224	1.169	224	1.174	405	1.188
	1.114	318, 028	1.116	406, 028	1.116, 1.113	31.12, 02.12	1.115

Note: $a = 4.945 \text{ \AA}$, $b = 2.855 \text{ \AA}$, $c = 14.320 \text{ \AA}$ ($2H$ polytype), $a = 5.060 \text{ \AA}$, $b = 2.855 \text{ \AA}$, $c = 14.200 \text{ \AA}$ ($2O$ polytype), and $a = 4.945 \text{ \AA}$, $b = 2.855 \text{ \AA}$, $c = 21.420 \text{ \AA}$ ($3R$ polytype). $\alpha = \beta = \gamma = 90^\circ$ for all three polytypes. Calculated $d_{\text{cal}} (hkl)$ reflection positions (in \AA) are compared to experimental $d_{\text{exp}} (hkl)$ ones.

Table 5. Indexing of the experimental XRD patterns of $\text{KBi}_{10\text{h}}$ and $\text{KBi}_{8\text{h}}$ recorded *in situ* at 350°C with a $2H$ cell.

hkl	350- $\text{KBi}_{10\text{h}}$		350- $\text{KBi}_{8\text{h}}$	
	$d_{\text{exp}} (hkl)$	$d_{\text{cal}} (hkl)$	$d_{\text{exp}} (hkl)$	$d_{\text{cal}} (hkl)$
002	6.471 4.818 ^a 4.332 ^a 4.124 ^a	6.460	6.506	6.498
004	3.231	3.230	3.248	3.249
200, 110	2.504	2.506	2.490	2.490
201, 111	2.462	2.460	2.423 ^b	
202, 112	2.336	2.337	2.326	2.325
203, 113	2.166	2.166	2.159 2.096 ^b	2.159
204, 114	1.980	1.980	1.976	1.976
205, 115	1.801	1.799	1.785 ^b	1.798
206, 116	1.634	1.633	1.634	1.634
008	1.618	1.615	1.618	1.624
310, 020	1.447	1.447	1.437	1.438
312, 022	1.412	1.412	1.403	1.404
208, 118			1.360	1.360
314, 024			1.313	1.315
400, 220			1.242	1.245
402, 222			1.221	1.223
316, 026			1.193	1.198
404, 224			1.152	1.162

Note: $a = 5.013 \text{ \AA}$, $b = 2.894 \text{ \AA}$, $c = 12.920 \text{ \AA}$ (350- $\text{KBi}_{10\text{h}}$ sample), and $a = 4.980 \text{ \AA}$, $b = 2.875 \text{ \AA}$, $c = 12.995 \text{ \AA}$ (350- $\text{KBi}_{8\text{h}}$ sample). $\alpha = \beta = \gamma = 90^\circ$ for the two samples. Calculated $d_{\text{cal}} (hkl)$ reflection positions (in \AA) are compared to experimental $d_{\text{exp}} (hkl)$ ones. ^a indicates unindexed additional weak lines. ^b indicates 11ℓ reflections of a $3R$ -type additional phase

Table 6. Optimum structural parameters (atomic positions and occupancies) used for the simulation of sample $\text{KBi}_{10\text{h}}$ with $2H$ and $2O$ polytypes.

	2H polytype				2O polytype			
	x	y	ζ (Å)	Occ.	x	y	ζ (Å)	Occ.
Mn_{layer}	0	0	0	0.98	0	0	0	0.98
O_{layer}	± 0.333	0	± 1.000	2.00	± 0.341	0	± 1.000	2.00
K	-0.220	0	3.560	0.09	-0.250	0	3.560	0.09
K	0.110	± 0.330	3.560	0.18	0.125	± 0.375	3.560	0.18
H_2O	0.150	0	3.560	0.17	0.150	0	3.560	0.53
H_2O	0.075	± 0.225	3.560	0.34	-	-	-	-

Note: Parameters defining the layer cation composition. Optimal values were determined by trial-and-error fitting of $\text{KBi}_{10\text{h}}$ experimental pattern (Figure 6d). x and y coordinates are expressed as fractions of the orthogonal a and b parameters, respectively. Coordinates along the c^* axis, ζ , are expressed in Å to emphasize the thickness of layer and interlayer polyhedra. $a = b\sqrt{3} = 4.976$ Å, $b = 2.873$ Å ($2H$ polytype – $P6_3/mmc$ space group), $a_1 = 5.124$ Å, $b_1 = 2.846$ Å, $a_2 = 5.101$ Å, $b_2 = 2.850$ Å, and $a_3 = 5.084$ Å, $b_3 = 2.853$ Å for the three $2O$ polytypes ($Cmcm$ space group). $c = 14.240$ Å, $\alpha = \beta = \gamma = 90^\circ$ for all 4 phases. Debye-Waller factors were 0.5, 1.0, 2.0, 2.0 for Mn_{layer} , O_{layer} , K and H_2O , respectively. Occupancies are given for the sum of all symmetrical sites. For all elementary contributions, the radius of the coherent scattering domains in the ab plane is 350 Å, whereas the mean coherent scattering domain along the c^* axis is 17 layers. All elementary contributions are devoid of random stacking faults.

Table 7. Selected inter-atomic distances calculated from the optimal atomic coordinates for KBi samples.

	KBi_{10h}				KBi_{8h} and KBi₇		
	<i>2O-1</i>	<i>2O-2</i>	<i>2O-3</i>	<i>2H</i>	<i>2O</i>	<i>2H</i>	<i>3R</i>
Height of Mn layer	2.00	2.00	2.000	2.000	2.000	2.000	2.000
Mn _{layer} -Mn _{layer}	2.846 x2 2.931 x4	2.850 x2 2.922 x4	2.853 x2 2.915 x4	2.873 x6	2.855 x2 2.905 x4	2.855 x6	2.855 x6
Average Mn _{layer} - Mn _{layer}	2.903	2.898	2.894	2.873	2.888	2.855	2.855
Mn _{layer} -O _{layer}	1.929 x4 2.023 x2	1.929 x4 2.016 x2	1.929 x4 2.011 x2	1.946 x6	1.927 x4 2.003 x2	1.940 x6	1.938 x6
Average Mn _{layer} - O _{layer}	1.960	1.958	1.956	1.946	1.952	1.940	1.938
Mn ³⁺ _{interlayer} -Mn _{layer}	-	-	-	-	-	3.512	3.509
Mn ³⁺ _{interlayer} -O _{layer}	-	-	-	-	-	1.940	1.938
Mn ³⁺ _{interlayer} - H ₂ O _{interlayer}	-	-	-	-	-	2.251	2.248
O _{layer} -H ₂ O _{interlayer}	-	-	-	-	-	3.043	3.037
K _{interlayer} -O _{layer}	2.951 x2 3.295 x1	2.952 x2 3.289 x1	2.952 x2 3.284 x1	2.933 x2 3.377 x1	2.929 x2 3.373 x1	2.933 x2 3.444 x1	2.927 x2 3.439 x1
Average K _{interlayer} - O _{layer}	3.066	3.064	3.063	3.081	3.077	3.103	3.098
K _{interlayer} - H ₂ O _{interlayer}	3.074 x1 3.507 x2	3.061 x1 3.505 x2	3.050 x1 3.504 x2	2.731 x2 3.135 x1 3.305 x1 3.412 x2	3.188 x1 3.414 x2	2.731 x2 3.223 x2 3.440 x2	2.731 x2 3.223 x2 3.440 x2
O _{layer} -H ₂ O _{interlayer}	2.725	2.723	2.722	2.702	-	2.730	2.723

Note: All distances are given in Å.

Table 8. Optimum structural parameters (atomic positions and occupancies) used for the simulation of sample KBi_{8h} and KBi_7 with $2H$, $2O$, and $3R$ polytypes.

	2H polytype				2O polytype				3R polytype			
	x	y	$\zeta(\text{\AA})$	Occ.	x	y	$\zeta(\text{\AA})$	Occ.	x	y	$\zeta(\text{\AA})$	Occ.
Mn_{layer}	0	0	0	0.85	0	0	0	0.98	0	0	0	0.85
O_{layer}	± 0.333	0	± 1.000	2.00	± 0.341	0	± 1.000	2.00	± 0.333	0	± 1.000	2.00
$\text{Mn}_{\text{interlayer}}$	0	0	± 2.100	0.11	-	-	-	-	0	0	± 2.100	0.11
$\text{H}_2\text{O}_{\text{inter.}}$	-0.333	0	3.580	0.33	-	-	-	-	-0.333	0	3.570	0.33
$\text{K}_{\text{inter.}}$	-0.200	0	3.580	0.09	-0.220	0	3.550	0.09	-0.200	0	3.570	0.045
$\text{K}_{\text{inter.}}$	0.100	± 0.300	3.580	0.18	0.110	± 0.330	3.550	0.18	0.100	± 0.300	3.570	0.09
$\text{K}_{\text{inter.}}$									-0.533	0	3.570	0.045
$\text{K}_{\text{inter.}}$									-0.233	± 0.300	3.570	0.09
$\text{H}_2\text{O}_{\text{inter.}}$	0.140	0	3.580	0.12	0.150	0	3.550	0.54	0.140	0	3.570	0.06
$\text{H}_2\text{O}_{\text{inter.}}$	-0.070	± 0.210	3.580	0.24					-0.070	± 0.210	3.570	0.12
$\text{H}_2\text{O}_{\text{inter.}}$									-0.193	0	3.570	0.06
$\text{H}_2\text{O}_{\text{inter.}}$									-0.263	± 0.210	3.570	0.12

Note: Parameters defining the layer cation composition. Optimal values were determined by trial-and-error fitting of KBi_{8h} and KBi_7 experimental pattern (Figures 9a, 10a). All notations as in Table 6. Debye-Waller factors are 0.5, 1.0, 1.5, 2.0, and 2.0 for Mn_{layer} , O_{layer} , $\text{Mn}_{\text{interlayer}}$, K and H_2O respectively. Occupancies are given for the sum of all symmetrical sites. For all elementary contributions, the radius of the coherent scattering domains in the ab plane is 350 \AA (300 \AA for the $2H/3R$ MLS with a high $2H$ content), whereas the mean coherent scattering domain along the c^* axis is 15 layers (20 layers for the $2O/2H$ MLS). All elementary contributions are devoid of random stacking faults.

Table 9. Unit-cell parameters of the elementary $2O$, $2H$, and $3R$ polytypes present in KBi samples.

		KBi _{8h} KBi ₇	KBi _{8o} ^a		KBi _{10h}		KBi _{10o} ^b
$2O$	a	5.060	-	5.124	5.101	5.084	5.155
	b	2.855	-	2.846	2.850	2.853	2.846
	a/b	1.772	-	1.800	1.790	1.782	1.811
	c	14.220	-		14.240		14.088
$2H$	a	4.945	4.928		4.976		-
	b	2.855	2.845		2.873		-
	a/b	1.732	1.732		1.732		-
	c	14.320	14.235		14.240		-
$3R$	a	4.945	-		-		-
	b	2.855	-		-		-
	a/b	1.732	-		-		-
	c	21.420	-		-		-

Note: All unit-cell parameters are given in Å. $\alpha = \beta = \gamma = 90^\circ$ for all phases. ^a Sample described by Gaillot et al.²⁴ ^b Sample described by Gaillot et al.²⁵

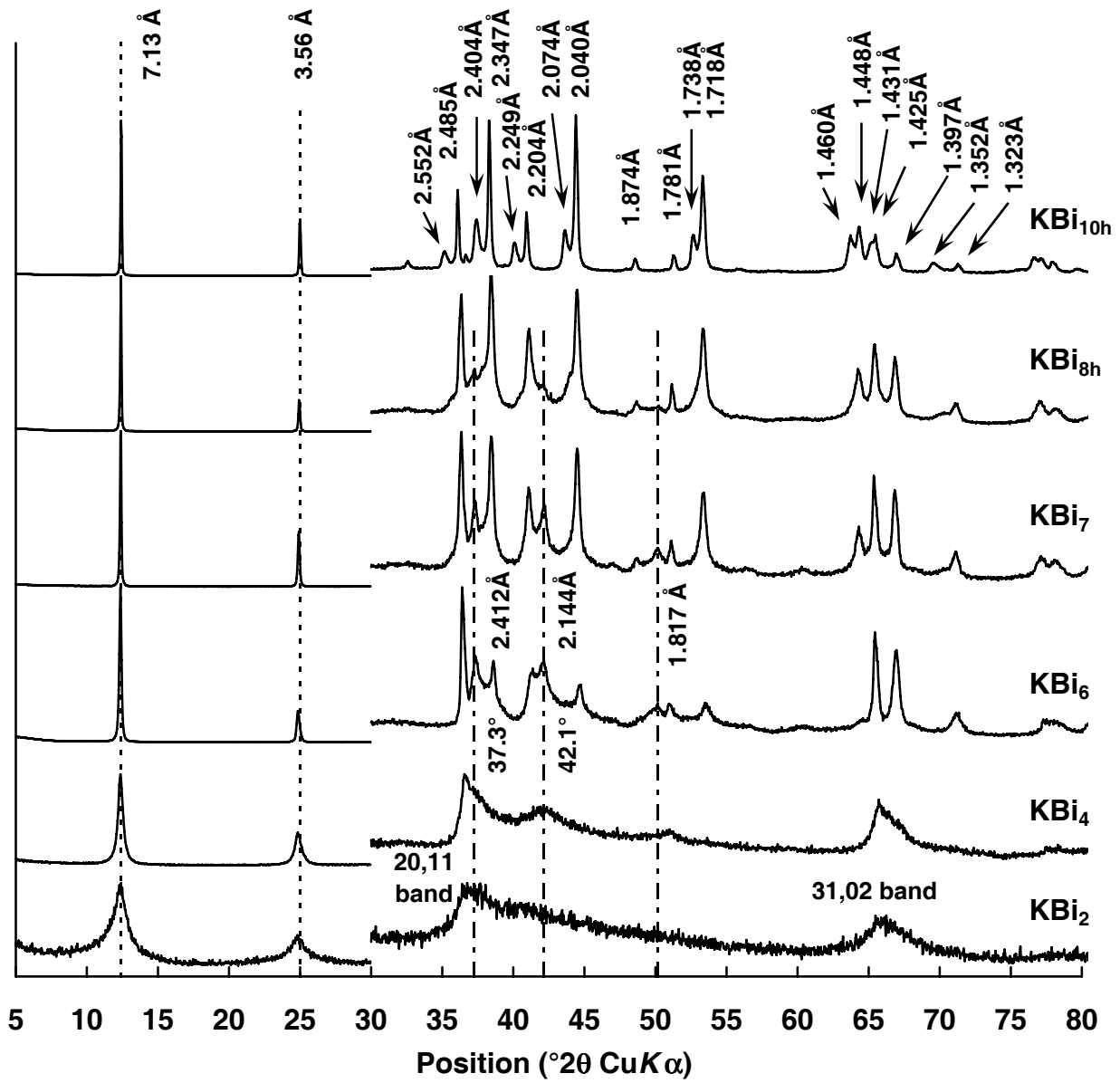
		350-KBi _{8h}	350-KBi _{10h}	350-KBi _{10o} ^c
$2H$	a	4.980	5.013	5.014
	b	2.875	2.894	2.895
	a/b	1.732	1.732	1.732
	c	12.995	12.920	12.848

Note: All unit-cell parameters are given in Å. $\alpha = \beta = \gamma = 90^\circ$ for all phases. ^c Sample described by Gaillot et al.²⁵

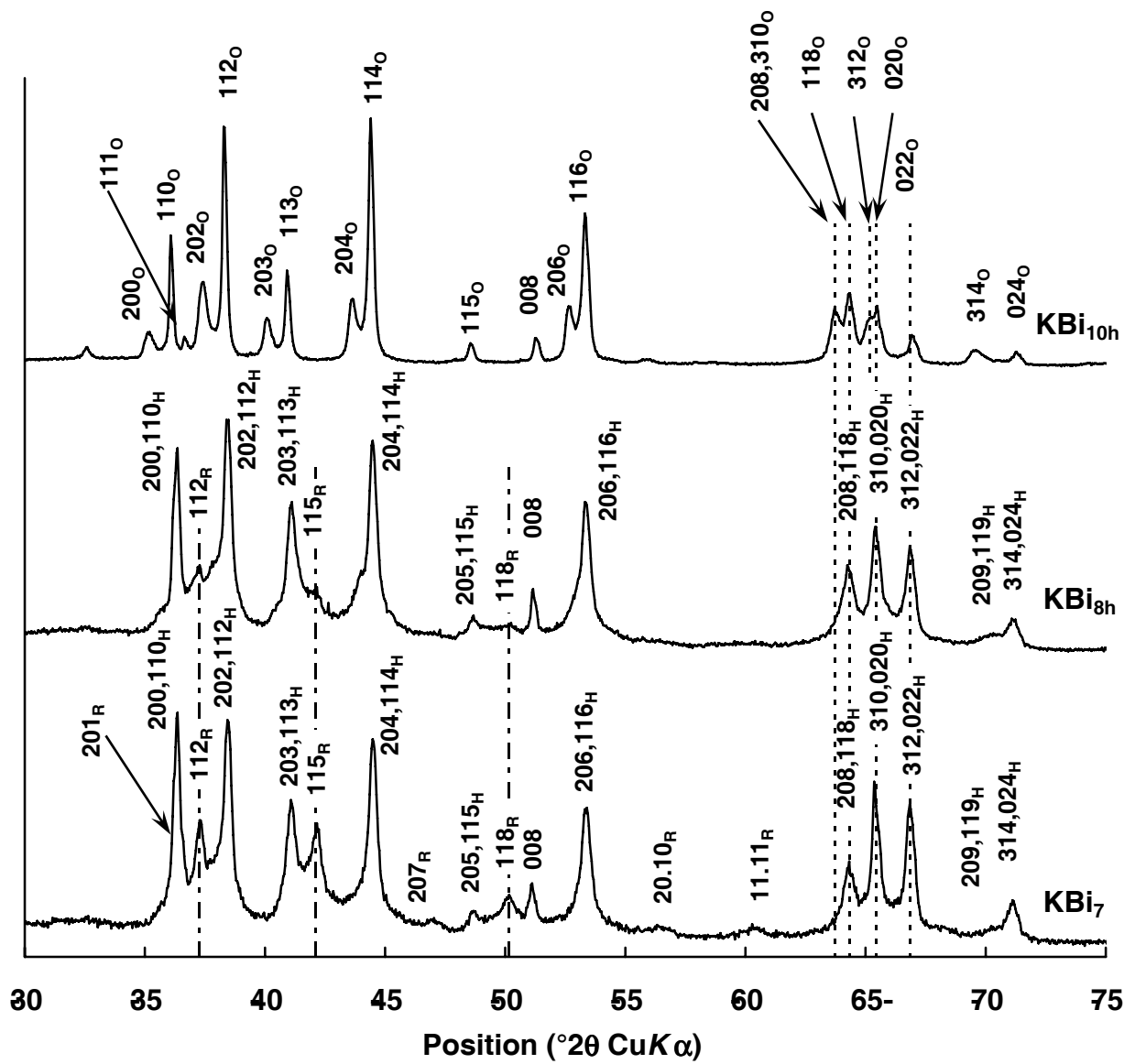
Table 10. Composition of the different elementary phases present in KBi samples.

	<i>3R/2H</i>		<i>2H/3R</i>		<i>2H</i>	<i>2O/2H</i>		<i>2O</i>	Total	
KBi ₇	23%		41%		7%	29%		-		
	<i>3R</i>	<i>2H</i>	<i>3R</i>	<i>2H</i>	<i>2H</i>	<i>2H</i>	<i>2O</i>	-	<i>2O</i>	15%
	90%	10%	30%	70%	100%	50%	50%	-	<i>2H</i>	53%
	21%	2%	12%	29%	7%	15%	15%	-	<i>3R</i>	33%
KBi _{8h}	8%		48%		9%	34%		-		
	<i>3R</i>	<i>2H</i>	<i>3R</i>	<i>2H</i>	<i>2H</i>	<i>2H</i>	<i>2O</i>	-	<i>2O</i>	20%
	85%	15%	25%	75%	100%	40%	60%	-	<i>2H</i>	60%
	7%	1%	12%	36%	9%	14%	20%	-	<i>3R</i>	19%
KBi _{10h}	-	-	-	-	24%	-	-	76%		
	-	-	-	-	<i>2H</i>	-	-	<i>2O</i>	<i>2O</i>	76%
	-	-	-	-	100%	-	-	100%	<i>2H</i>	24%
	-	-	-	-	24%	-	-	76%	<i>3R</i>	0%

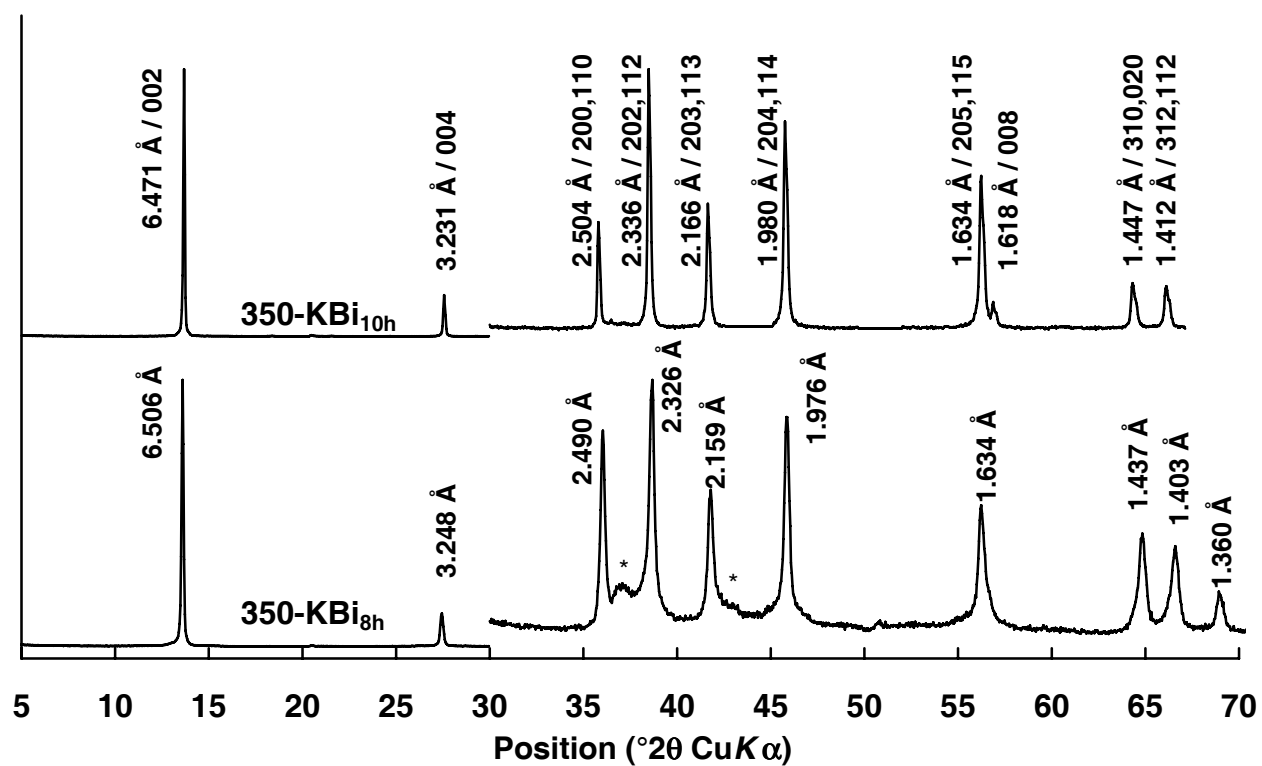
Note: For KBi_{10h}, all contributions from *2O* polytypes with different unit cell parameters are all summed up.



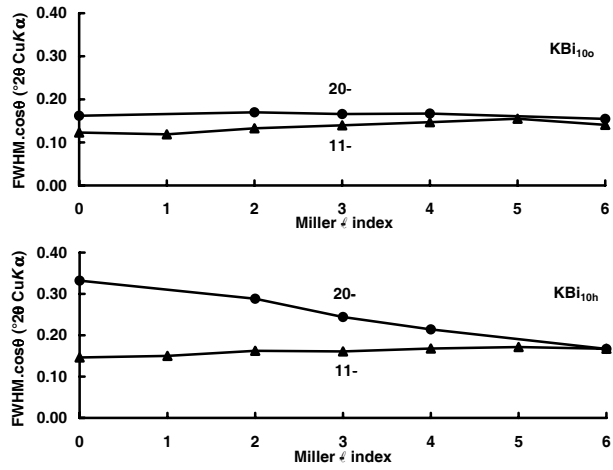
Please print in two column format



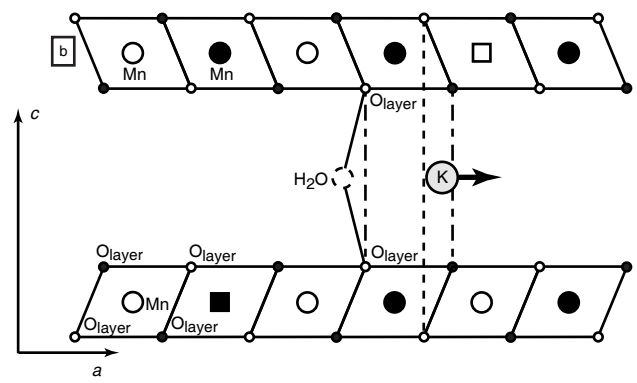
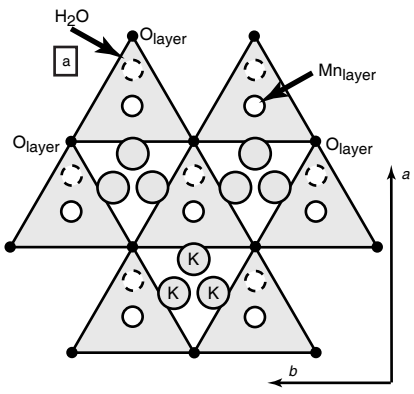
Please print in two column format



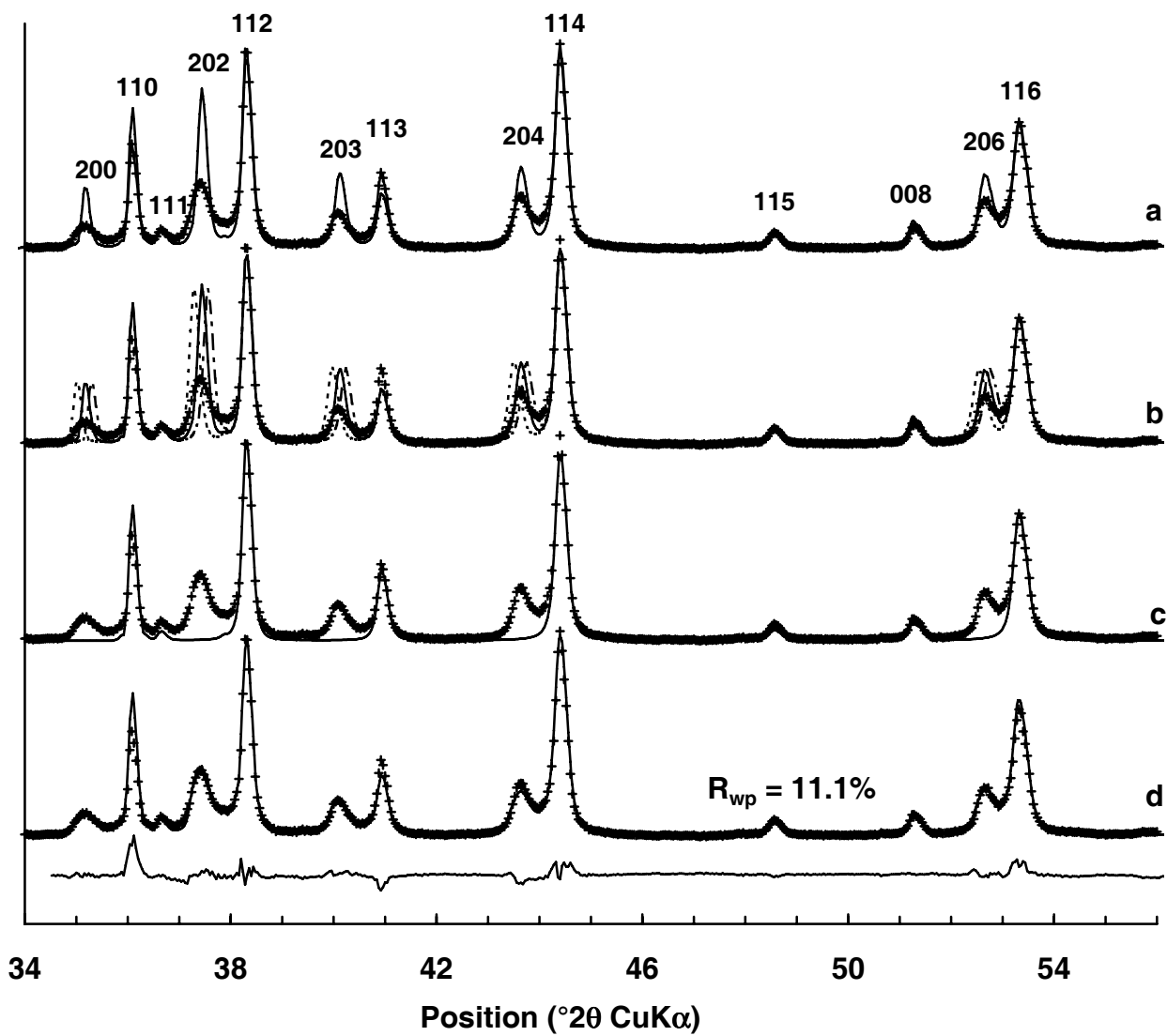
Please print in two column format



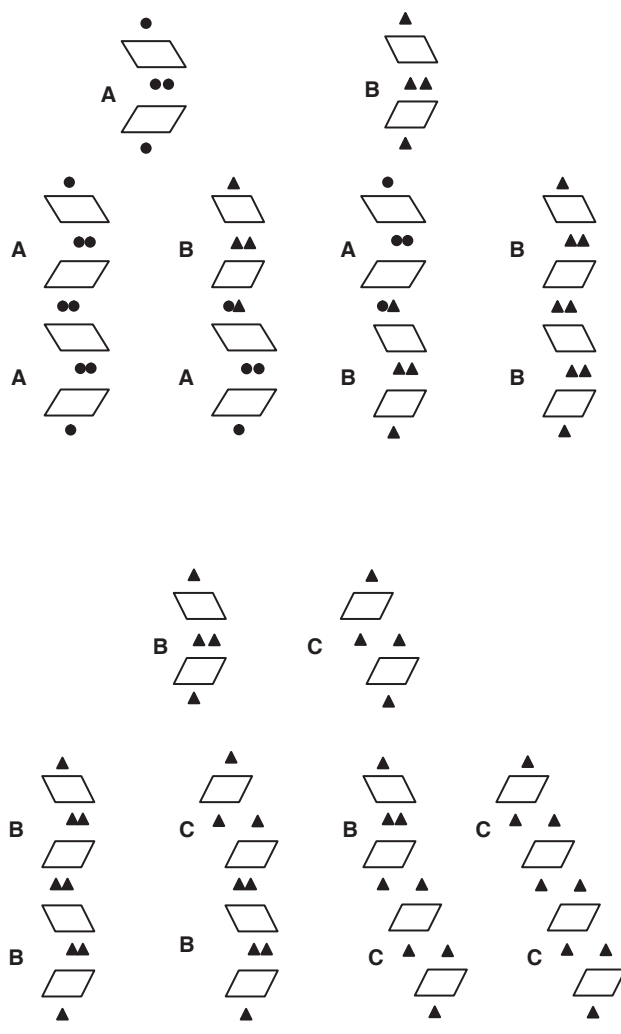
Please print in one column format



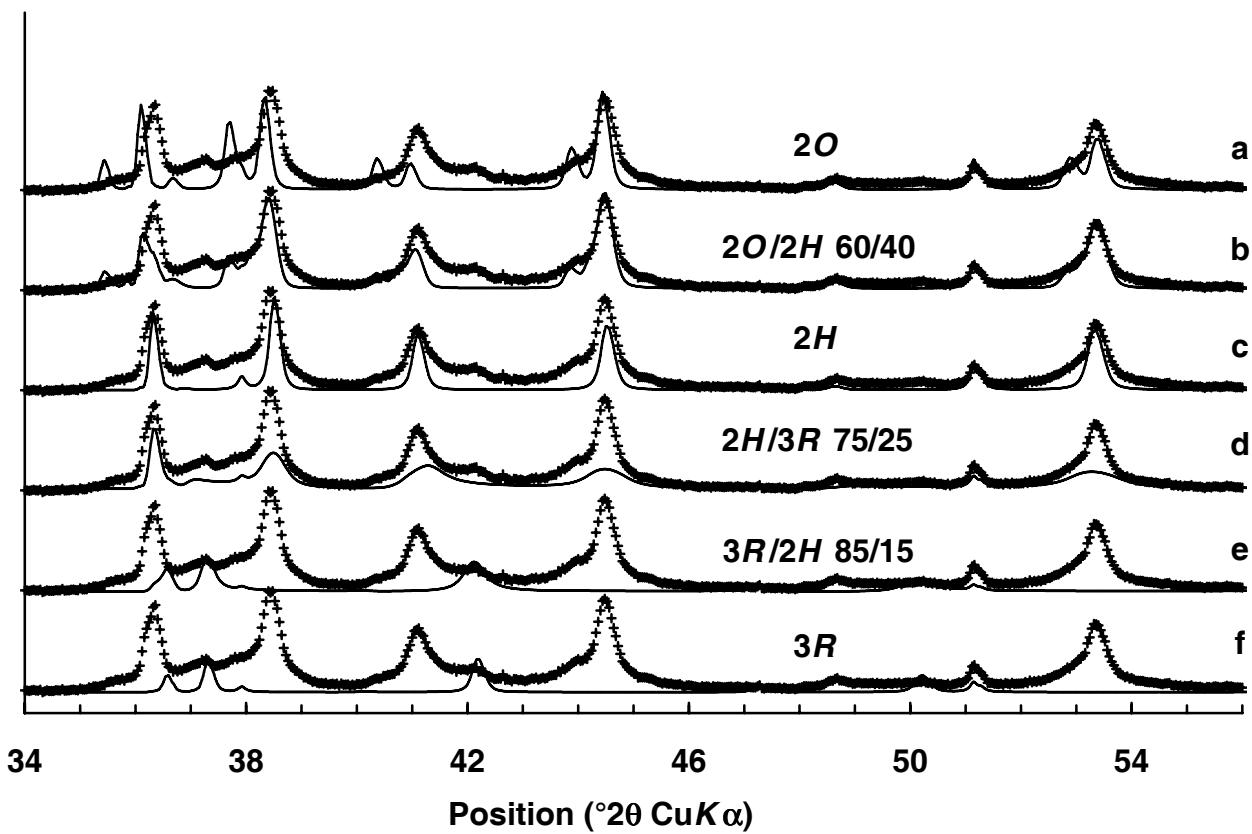
Please print in one column format



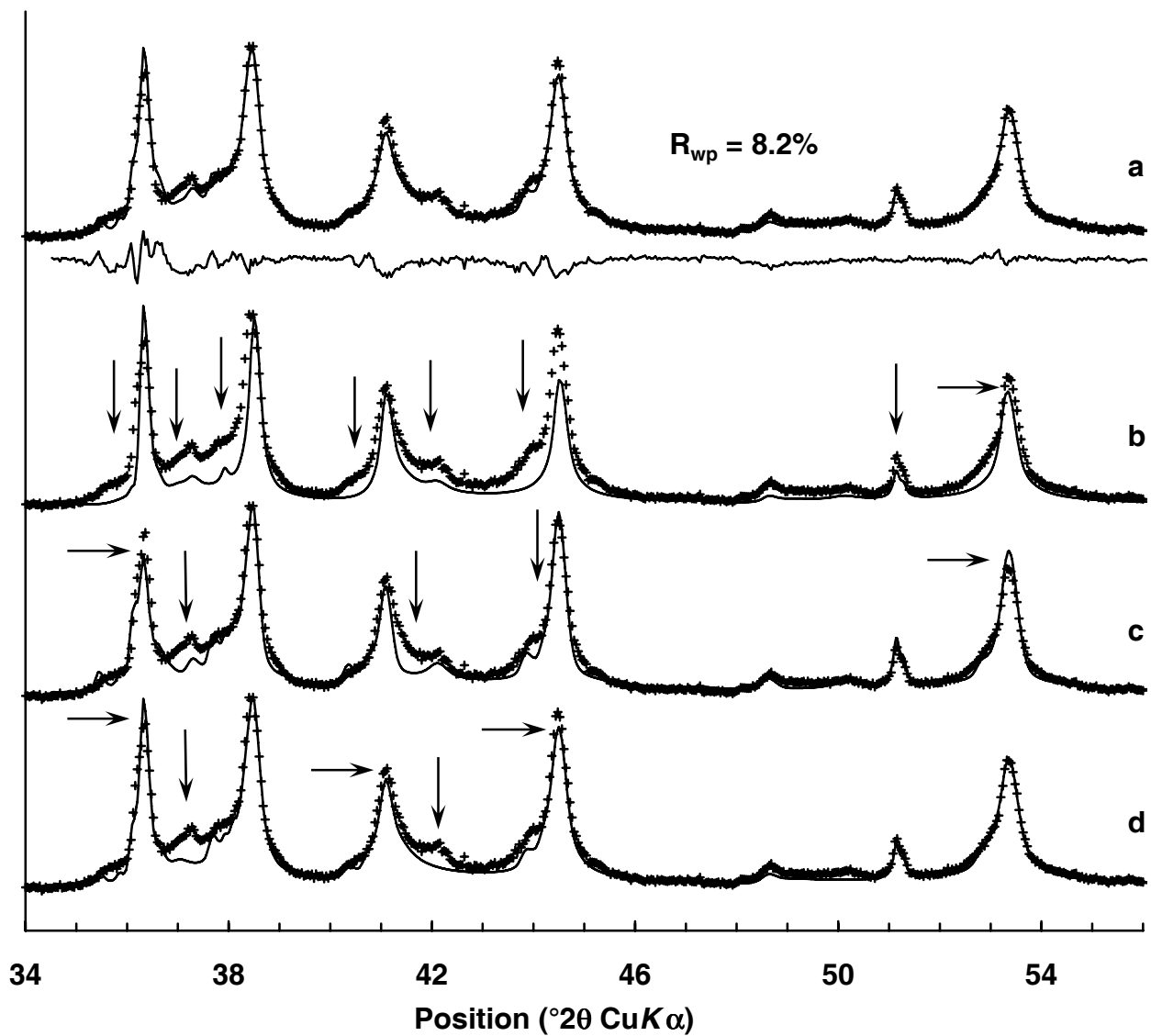
Please print in two column format



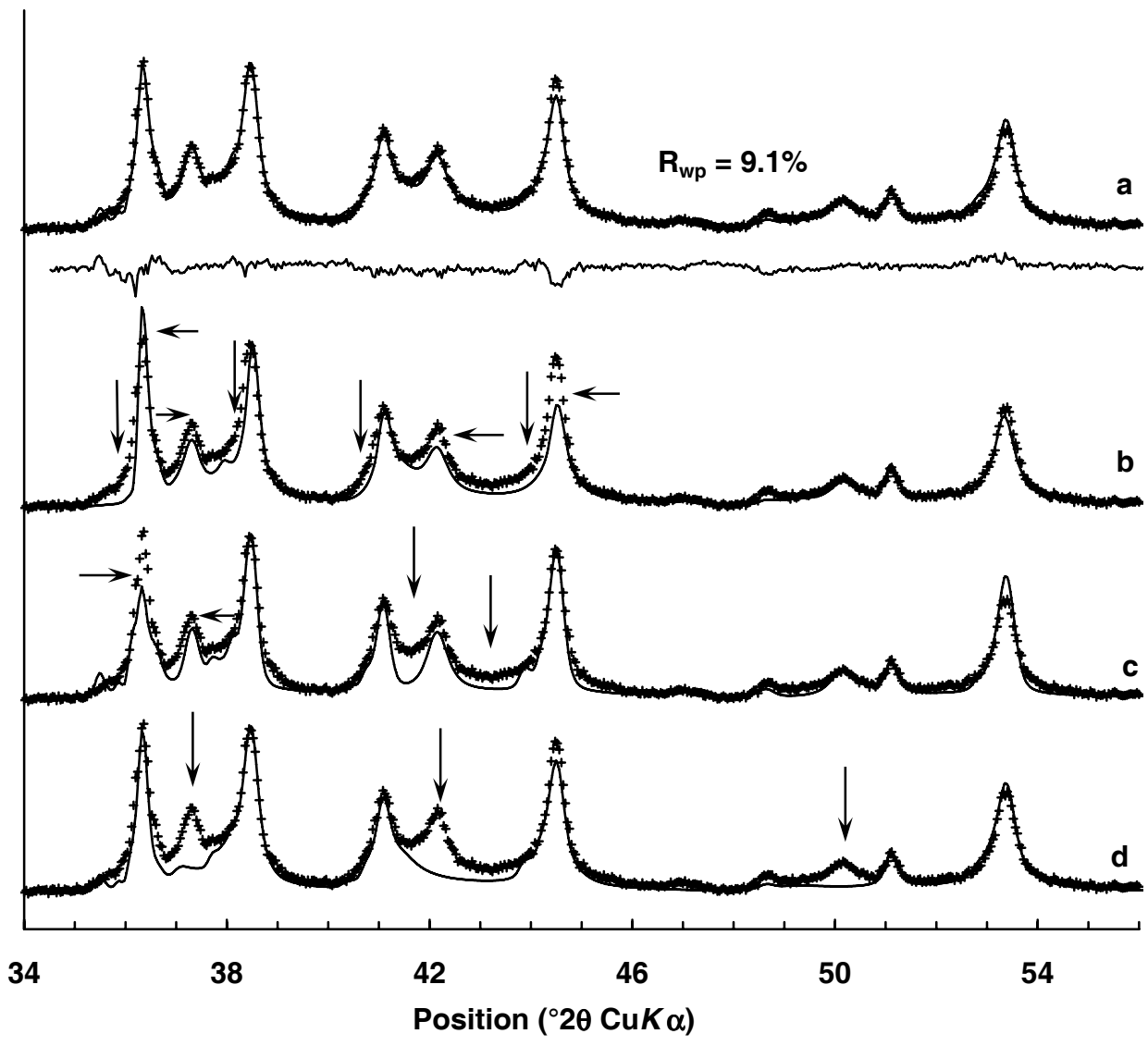
Please print in one column format



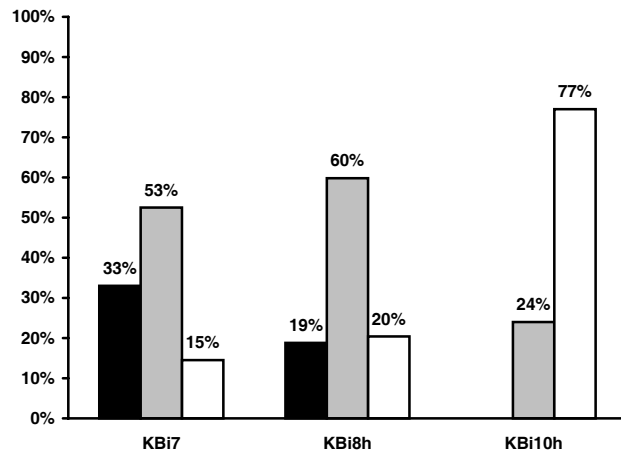
Please print in two column format



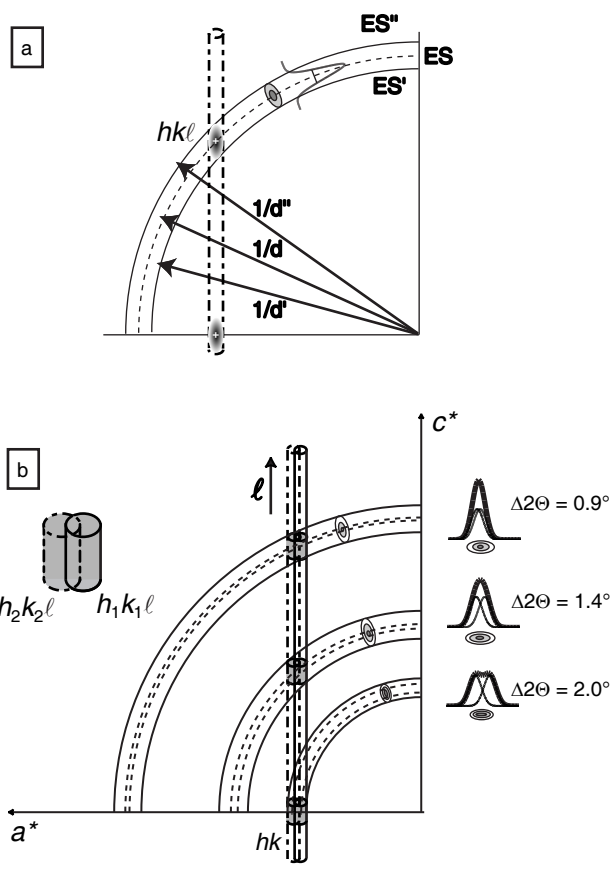
Please print in two column format



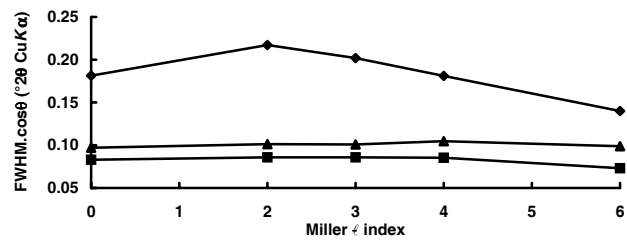
Please print in two column format



Please print in one column format



Please print in one column format



Please print in one column format